

XMM-Newton observations of the Lockman Hole: X-ray source catalogue and number counts^{*}

H. Brunner¹, N. Cappelluti¹, G. Hasinger¹, X. Barcons², A. C. Fabian³, V. Mainieri^{1,4} and G. Szokoly¹

¹ Max-Planck-Institut für extraterrestrische Physik, 85478 Garching, Germany

² Instituto de Física de Cantabria (CSIC-UC), 39005 Santander, Spain

³ Institute of Astronomy, University of Cambridge, Madingley Road, Cambridge, CB3 0HA

⁴ ESO, Karl-Schwarzschild-Strasse 2, 85748 Garching, Germany

Received ; accepted

ABSTRACT

Context. The Lockman Hole field represents the sky area of lowest Galactic line-of-sight column density $N_{\text{H}}=5.7\times10^{19} \text{ cm}^{-2}$. It was observed by the XMM-Newton X-ray observatory in 18 pointings for a total of 1.16 Msec (raw EPIC pn observing time) constituting the deepest XMM-Newton exposure so far. After the removal of time intervals with high particle background, the final effective exposure was 637 ks.

Aims. We present a catalogue of the X-ray sources detected in the central 0.196 deg^2 of the field and discuss the derived number counts and X-ray colours.

Methods. The analysis was performed using the XMM-SAS data analysis package version 6.0. The detection sensitivity and fraction of spurious detections was calibrated using Monte Carlo simulations.

Results. In the 0.5–2.0 keV band, a sensitivity limit (defined as the faintest detectable source) of $1.9\times10^{-16} \text{ erg cm}^{-2} \text{ s}^{-1}$ was reached. The 2.0–10.0 keV band and 5.0–10.0 keV band sensitivity limits were $9\times10^{-16} \text{ erg cm}^{-2} \text{ s}^{-1}$ and $1.8\times10^{-15} \text{ erg cm}^{-2} \text{ s}^{-1}$, respectively. A total of 409 sources above a detection likelihood of 10 (3.9 sigma) were found within a radius of 15' off the field centre, of which 340, 266, and 98 sources were detected in the soft, hard, and very hard bands, respectively. The number counts in each energy band are in close agreement with results from previous surveys and with the synthesis models of the X-ray background. A 6% of Compton-thick source candidates have been selected from the X-ray colour-colour diagram. This fraction is consistent with the most recent predictions of X-ray background population synthesis models at our flux limits. We also estimated, for the first time, the logN-logS relation for Compton-thick AGN.

Key words. survey – galaxies: active – galaxies: quasars: general – X-ray: galaxies – X-rays: general

1. Introduction

Due to its extremely low line of sight column density of $N_{\text{H}}=5.7\times10^{19} \text{ cm}^{-2}$, the Lockman Hole field is one of the main extragalactic deep-survey target areas of recent X-ray observatories. The choice of a low N_{H} field on the one hand optimizes the soft-band sensitivity compared to fields with higher N_{H} . An even more important aspect is that for many sources we can determine spectra to the lowest possible energies and thus get a better handle on the continuum and intrinsic absorption.

The field was observed for a total of 1.1 Msec, by the ROSAT HRI detector, reaching a sensitivity limit of $1.2\cdot10^{-15} \text{ erg cm}^{-2} \text{ s}^{-1}$ in the 0.5–2.0 keV band, for the first time resolving the majority of the soft X-ray background into discrete sources (Hasinger et al. 1998). The Lockman Hole was also the target of the deepest observations conducted by the XMM-Newton observatory, considerably improving the sensitivity limit in the soft band and extending the survey into the hard X-ray band up to an energy of 10 keV. Although the sensitivity limit of the XMM-Newton Lockman Hole survey does not reach the sensitivity of the deepest surveys performed by the *Chandra* observatory (i.e. the *Chandra* deep field North and South, Bauer et al.

2004, Giacconi et al. 2001), the larger collecting area of XMM-Newton offers the possibility to perform a spectral analysis of a large fraction of the detected sources down to the confusion limit, opening up a powerful window into the cosmological evolution of the X-ray universe.

The Lockman Hole field dataset allowed us for example to study the Fe K line emission of one of the most distant X-ray selected cluster of galaxies, RX J1053.7+5735I. Hashimoto et al. (2004) were able to determine the X-ray redshift of the cluster and its metallicity. The XMM-Newton Lockman Hole survey is also well suited to investigate the X-ray spectra and cosmological evolution of both absorbed and unabsorbed AGN. With its large collecting area, XMM-Newton is able to obtain detailed spectral information even for the faintest sources. Mainieri et al. (2002) and Mateos et al. (2005) performed a detailed spectral analysis and they discovered several candidate Compton thick AGNs. According to the recent model of Gilli et al. (2007), 40% of the flux of the X-ray background is expected to arise in highly absorbed AGNs ($N_{\text{H}} > 10^{22} \text{ cm}^{-2}$). These sources are mostly faint and detectable with deep X-ray surveys such as the XMM-Newton Lockman Hole survey. Worsley et al. (2004) estimated that the XMM-Newton Lockman Hole observations resolve ~100% of the soft X-ray background into discrete sources while at energies above 5 keV this fraction drops to ~50%. The missing part therefore could be due to very faint, highly absorbed AGNs ($N_{\text{H}} > 10^{22} \text{ cm}^{-2}$) to which XMM-Newton is not sensitive.

Send offprint requests to: H. Brunner, e-mail: hbrunner@mpe.mpg.de

* Based on observations obtained with XMM-Newton, an ESA science mission with instruments and contributions directly funded by ESA Member States and NASA

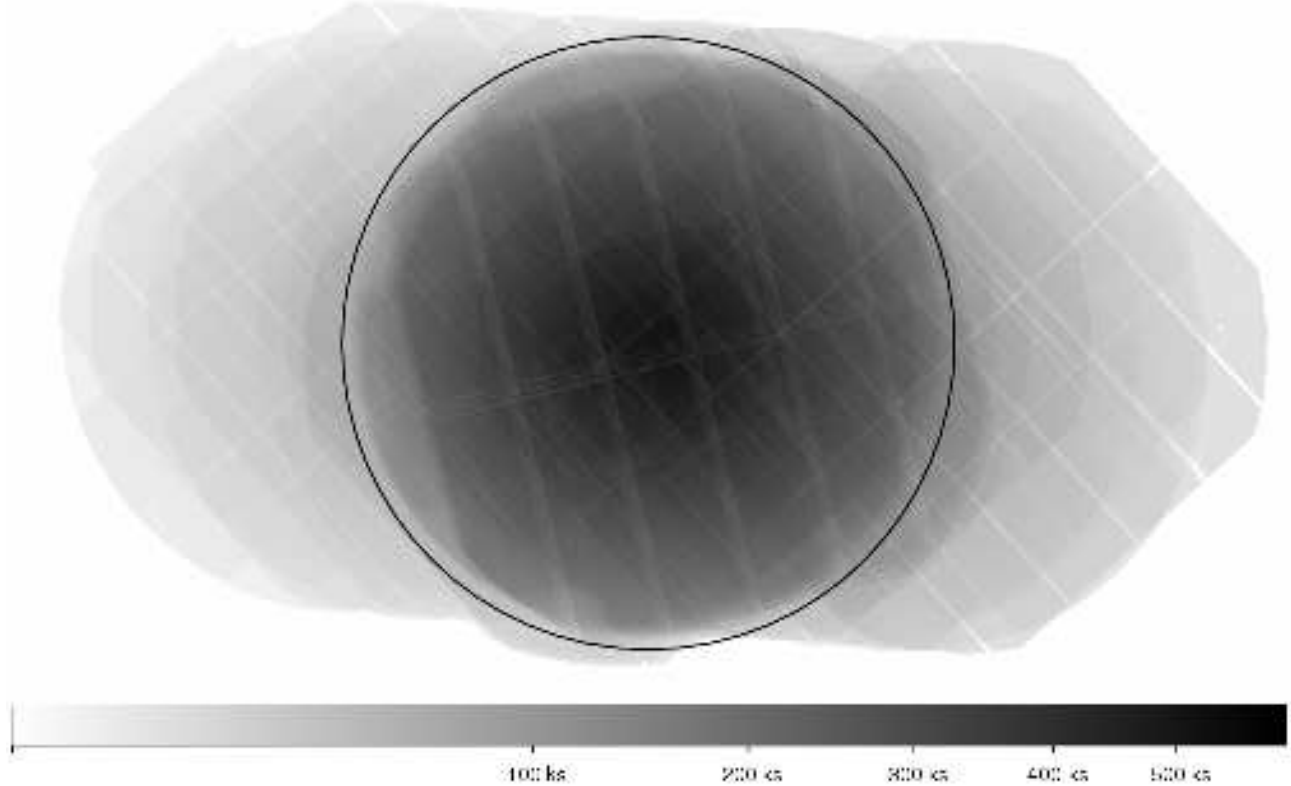


Fig. 1. Combined all-EPIC vignetting-corrected soft band exposure map of 18 XMM-Newton pointings on the Lockman Hole field. The black circle represents the region of 15' radius under investigation.

2. Observations

The Lockman Hole field was observed by XMM-Newton in 18 individual pointings distributed over a two and a half year time period from April 2000 to December 2002. Twelve pointings were centred at the approximate field centre coordinates $+10^h 52^m 43^s$, $57^\circ 28' 48''$ (J2000), with small offsets $\sim 15''$ to achieve an adequate coverage of the sky area falling into chip gaps in individual observations. The remaining pointings were spread out over about 30' in right ascension, thus covering a somewhat wider area at intermediate exposure levels. The pattern of the observations is shown in the vignetting corrected exposure map of Fig. 1 (see next section). The total XMM-Newton exposure time spent on the field was 1.30 Msec (EPIC MOS detectors; EPIC pn detector: 1.16 Msec). After removal of times affected by background flares 765 ks (EPIC MOS detector; EPIC pn detector: 637 ksec) are left which are suitable for scientific analysis. If the loss of sensitivity at large off-axis angles due to vignetting is considered, the average exposure time is reduced to 557.6 ks (weighted average of MOS and pn detectors). This paper addresses the sky area within 15' of the field centre where the exposure exceeds 185 ks. Table 1 lists the pointing directions and exposure times. The twelve central pointings and East and West offset pointings are marked by C, E, and W, respectively.

3. Data reduction

Event calibration was performed by uniformly processing all 18 data sets using the XMM-SAS 6.0 software package¹. Times affected by background flares were screened out by using a 3σ

clipping method, resulting in the clean exposure times listed in table 1. Out-of-time event² files were processed in the same way as the data and subtracted from our observations. In order to achieve the full sensitivity, data from all three XMM-Newton cameras of all observations were co-added on a joint sky-pixel grid of 3" pixels after performing astrometric corrections of each individual dataset based on highly accurate source positions from ROSAT optical follow-up work. The standard XMM-SAS source detection package was used to perform source detection on the area within 15' from the field centre of the co-added data in the energy bands 0.5–2.0 keV, 2.0–4.5 keV and 4.5–10.0 keV. The spectral range between 7.8 and 8.2 keV, affected by instrumental Cu line background emission, was excluded from the EPIC pn camera 4.5–10 keV images to improve the detection sensitivity in that band.

Unless otherwise stated we analyzed the data in the three non-overlapping energy bands 0.5–2.0 keV, 2.0–4.5 keV, and 4.5–10.0 keV. The fluxes measured in these energy bands were extrapolated to the canonical 0.5–2 keV, 2–10 keV, and 5–10 keV bands, respectively, by assuming a power-law spectrum with spectral index $\Gamma = 2$ and galactic $N_{\text{H}} = 5.7 \times 10^{19} \text{ cm}^{-2}$. For the sake of clarity we will call these energy bands soft, hard, and very hard band, respectively. The 0.5–10.0 keV energy band will be referred to as full band.

Exposure maps were computed in the same energy bands as the images. Since this work has been conducted using co-added EPIC MOS and pn data, the exposure maps were weighted and co-added according to the respective energy conversion factors, computed from the instrument response matrices, again assum-

¹ Available from the XMM-Newton Science Operation Centre at <http://xmm.vilspa.esa.es/>.

² X-ray events hitting the detector during read-out resulting in a loss of positional information in the read-out direction.

Table 1. Pointing directions and exposure times

rev. ^a	OBS_ID ^b		RA (J2000) hh mm ss	DEC ° ′ ″	offset ^c '	MOS exposure times ^d [ksec]	pn
070	0123700101	C ^e	10 52 41.0	57 27 07	1.7	43.9 (33.7)	46.6 (33.6)
071	0123700201	C	10 52 42.4	57 27 16	1.5	61.0 (38.0)	55.9 (31.8)
073	0123700401	C	10 52 41.7	57 27 06	1.7	15.0 (12.9)	16.4 (13.2)
074	0123700901	C	10 52 41.1	57 27 17	1.5	15.0 (4.5)	14.0 (4.5)
081	0123701001	C	10 52 40.1	57 27 19	1.7	36.4 (25.7)	37.2 (25.6)
344	0022740101	C	10 52 45.6	57 30 27	1.8	83.3 (0.3)	75.3 (0.0)
345	0022740201	C	10 52 46.1	57 30 28	1.7	63.9 (23.6)	61.2 (26.9)
349	0022740301	C	10 52 43.9	57 30 27	1.7	37.7 (33.5)	36.4 (29.0)
522	0147510101	W	10 51 05.6	57 29 33	13.1	92.6 (69.8)	91.0 (52.5)
523	0147510801	W	10 51 29.8	57 29 50	9.9	77.2 (39.4)	75.7 (18.7)
524	0147510901	C	10 52 44.8	57 30 26	1.7	90.2 (40.6)	88.5 (18.9)
525	0147511001	W	10 52 10.4	57 30 15	4.6	83.4 (75.7)	81.9 (63.1)
526	0147511101	E	10 53 20.3	57 30 52	5.4	97.2 (34.9)	93.4 (24.2)
527	0147511201	E	10 54 00.4	57 31 09	10.7	101.5 (28.2)	100.5 (21.9)
528	0147511301	E	10 54 31.9	57 31 30	14.9	85.0 (22.2)	82.5 (15.2)
544	0147511601	C	10 52 38.7	57 30 26	2.0	124.9 (102.7)	121.1 (95.8)
547	0147511701	C	10 52 40.6	57 28 29	1.4	100.4 (96.5)	98.8 (91.4)
548	0147511901	C	10 52 41.0	57 30 45	2.0	90.4 (82.9)	88.8 (71.0)

^a XMM-Newton orbit number (revolution)^b XMM-Newton observation ID^c offset from field centre $+10^h 52^m 43^s$, $57^\circ 28' 48''$ ^d raw (after flare screening)^e central (C) pointings, East (E), and West (W) offset pointings

ing a power-law spectral index of $\Gamma = 2.0$ and $N_{\text{H}}=5.7 \times 10^{19} \text{ cm}^{-2}$. The combined all-EPIC exposure map of the 18 observations of the Lockman Hole field is displayed in Fig. 1. The displayed exposures include corrections for telescope vignetting (here displayed for the soft band). The circle marks the $15'$ radius area discussed in this paper.

The large variety of spectral properties of the source population is demonstrated in the false colour image of the field (Fig. 2), displaying exposure corrected and background subtracted count rates of the soft, hard, and very hard energy bands in the colours red, green, and blue, respectively. While the distribution of spectral types as indicated by the colour images appears wide, Mateos et al. (2005) and Mainieri et al. (2002 and 2007) in the Lockman Hole and Hasinger et al. (2007) in the COSMOS Field showed that the spectra of the X-ray sources have an average photon index $<\Gamma> \sim 2$. The choice of modeling the average spectrum with a power-law with spectral index $<\Gamma>=2$ and $N_{\text{H}}=5.7 \times 10^{19} \text{ cm}^{-2}$ for estimating the fluxes is therefore consistent with a detailed spectral analysis.

The considerable fraction of blue and green objects mainly represents the population of absorbed AGN in the field. A quantitative analysis of the X-ray colours based on the hardness ratios determined from the source count rates in each energy band is presented in section 4.4. Also note the clearly visible population of extended objects, including the distant double cluster RX J1053.7+5735 (Hashimoto et al. 2004 and 2005) in the upper left part of the image (source numbers 461 and 472; Fig. 3, tables 3 and 4). The source parameters of the detected extended objects are also discussed in section 4.4.

4. Data analysis

4.1. Maximum likelihood multi-stage source detection

Source detection was performed simultaneously on the soft, hard, and very hard band images using the *eboxdetect* and *emldetect* tasks of the XMM-SAS data analysis package. In the following section we briefly describe the XMM-SAS source detection procedure; see the XMM-SAS documentation¹ for additional details.

The source detection procedure consists of three consecutive detection steps. An initial source list is created by running a sliding box detection algorithm (XMM-SAS task *eboxdetect*) with detection box sizes 5×5 , 10×10 , and 20×20 pixels ($15'' \times 15''$, $30'' \times 30''$, and $60'' \times 60''$), where the local background is estimated from pixels adjacent to the detection box. The global background is determined by fitting a combination of vignetted and non-vignetted background components to the source free regions (as determined from the initial source list). The *eboxdetect* detection task is then rerun using the global background model for improved detection sensitivity, creating a list of source candidates down to a low statistical significance level ($\sim 2\sigma$). This list is fed into the *emldetect* task which performs a Maximum Likelihood fit of the distribution of source counts (based on the Cash C-statistics approach, Cash 1979), using a point spread function model obtained from ray tracing calculations (medium accuracy model from the XMM-Newton calibration database), creating the final source list of best-fit source positions and fluxes. The fit is performed simultaneously in all energy bands by summing the likelihood contributions of each band. Sources exceeding the detection likelihood threshold in the full band are regarded as detections; the catalogue is thus full band selected, i.e., it also includes very weak sources which do not exceed the detection threshold in any of the individual bands. Alternatively, it is possible that a weak source which slightly ex-

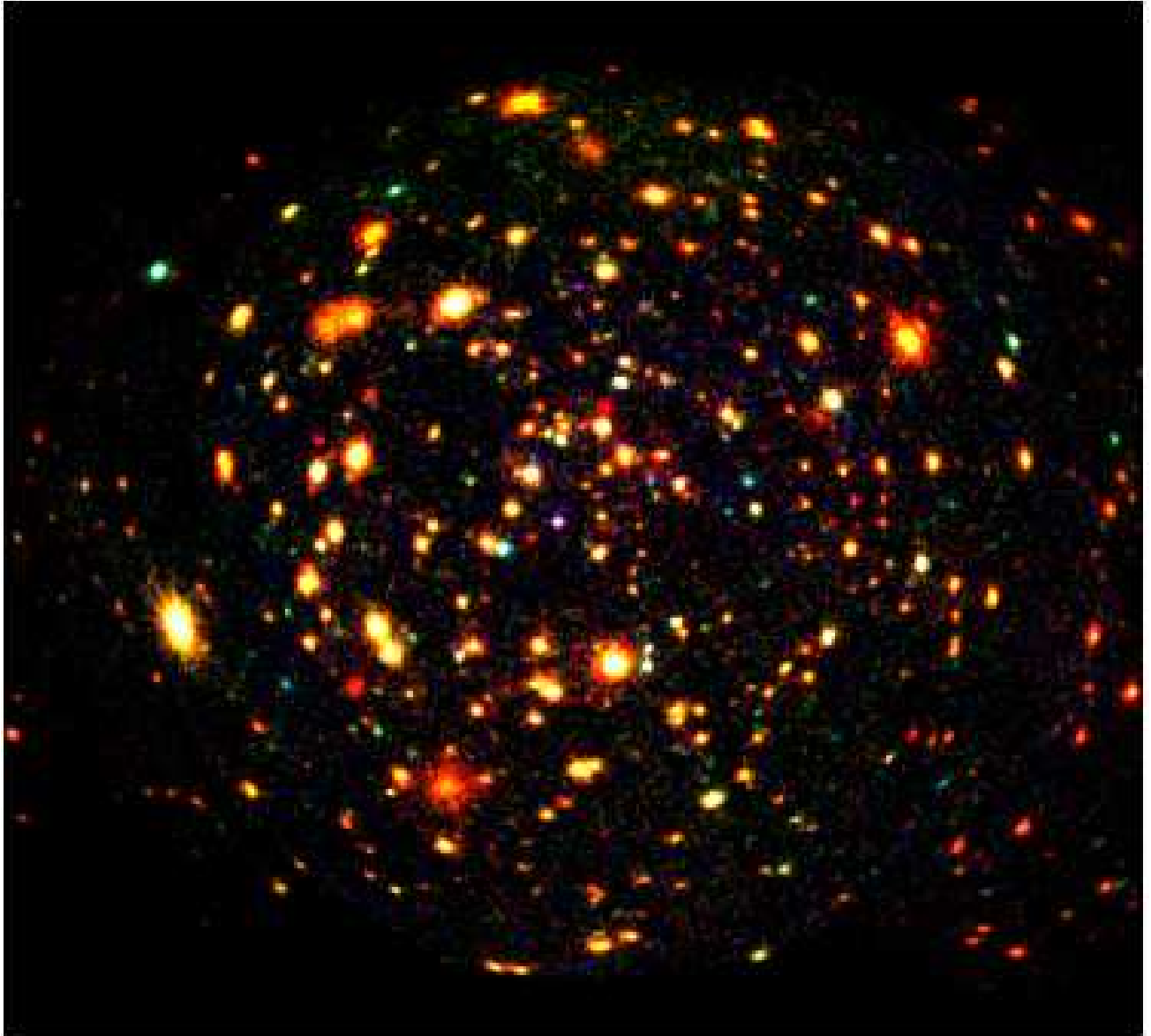


Fig. 2. Exposure corrected and background subtracted false colour image. The colours red, green, and blue code the 0.5–2.0 keV, 2.0–4.5 keV, and 4.5–10 keV fluxes, respectively. North is at the top, East is to the left. The image is centred on $10^h 52^m 43^s$, $57^\circ 28' 48''$ (J2000) and the field size is approximately $30' \times 30'$.

ceeds the detection threshold in one energy band and is not detected in the other bands may be excluded from the catalogue because it does not reach the detection threshold in the total band. A detection likelihood threshold of 10 was used for inclusion of detected objects into the source catalogue while objects with detection likelihoods above 6 were considered for determining the number counts (see details in section 4.3 and 4.4). The C-statistics approach can also be used to calculate the likelihood of the source extent. The best-fit parameters determined for each detected source thus are the source position, fluxes in each energy band and, optionally, the source extent (expressed as the core radius of a King profile). In the latter case, for each source, the distribution of source counts is modelled by numerically folding the point spread function with a King profile. The significance of detection in the total band and in each individual energy band is expressed in the form of a detection likelihood, \mathcal{L} , normalized to two degrees of freedom, obeying the relationship $\mathcal{L} = -\ln(p)$, where p is the probability that the observed

source counts are due to Poissonian fluctuations³. In principle the expected number of spurious sources is thus defined as the number of independent trials $\times p$ with $p = e^{-\mathcal{L}}$. The number of trials can be approximated by the number of point spread function sized beams in the field. This relationship is displayed as a straight line in Fig. 4 (see section 4.2 for details). However, due to the complex nature of the multi-step detection procedure, this relationship can only be regarded as a rough approximation which needs to be calibrated by Monte Carlo simulations (see section 4.2). A detailed description of the Maximum Likelihood source detection method can also be found in Cappelluti et al. (2007).

³ Note, that due to the higher number of degrees of freedom in the total band (one additional degree of freedom per band), the sum of the individual band detection likelihoods exceeds the total band detection likelihood by about 2.1.

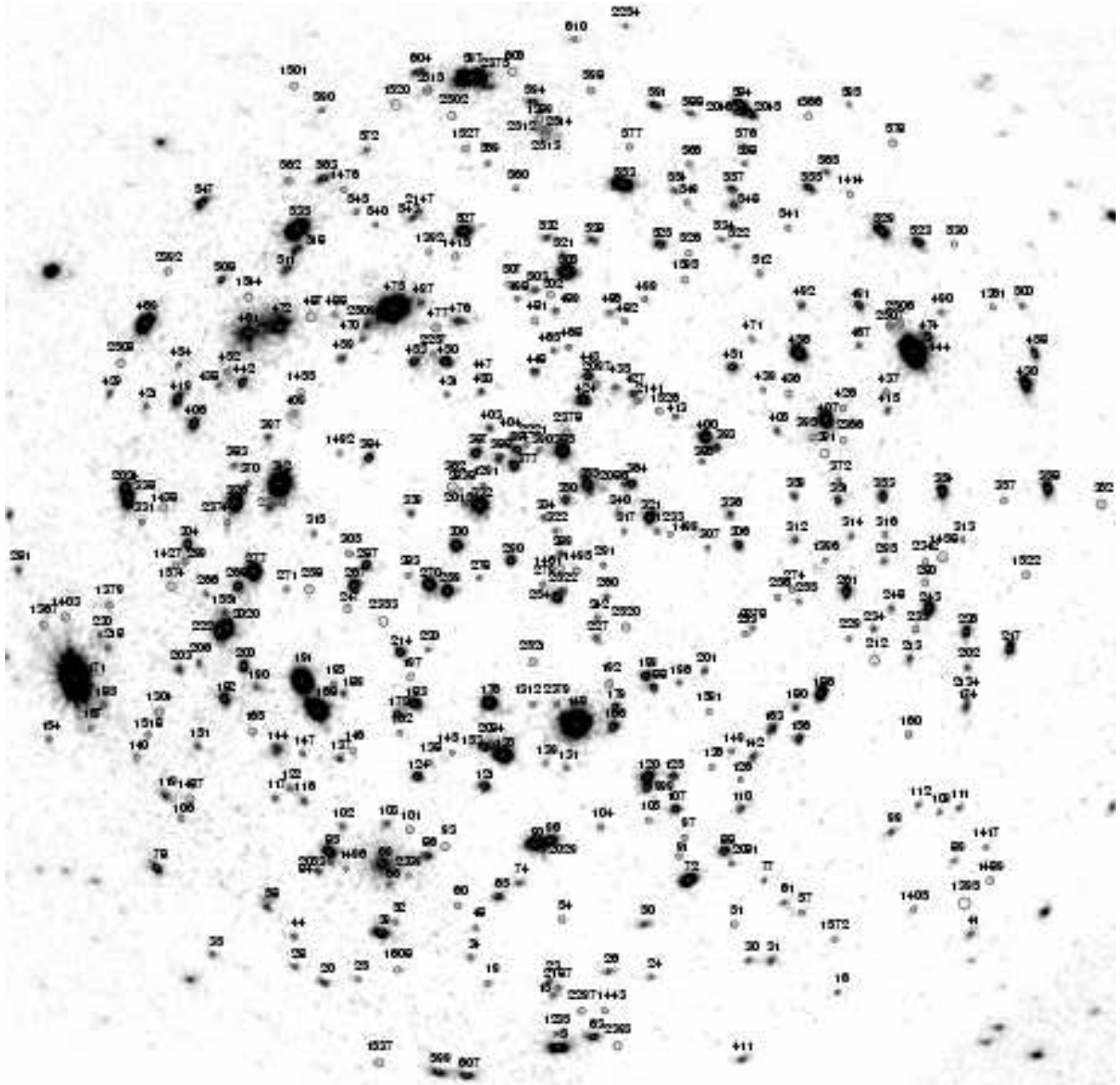


Fig. 3. Background subtracted full band image. Detected sources are marked by their 1σ positional error circle and source number. Field size and orientation as in Fig. 2.

4.2. Monte Carlo simulations

The behaviour of the detection procedure was verified by Monte Carlo simulations. We created 50 simulated fields in the soft, hard, and very hard energy band, each with the same sky exposure distribution and background level, with random source populations following a standard logN-logS distribution and the same spectral model as assumed for computing the exposure maps.⁴ In order to properly model the source confusion, sources were simulated down to a soft flux of 3×10^{-19} erg cm $^{-2}$ s $^{-1}$. The point spread function of the simulated sources was constructed from ray-tracing derived point spread function maps available in the XMM-Newton calibration database and by as-

suming the same pointing pattern as in the observations. The simulated point spread function thus closely matches the observed one at each image location. We subjected the simulated fields to the same source detection procedure as used for analyzing the observations. The 50 output catalogues were matched independently with the respective input catalogues. Sources with no corresponding simulated input were classified as spurious. We obtained the fraction of spurious sources by summing the number of spurious sources in each output catalogue and by normalizing to the total number of detected sources. Fig. 4 shows the number of spurious detections for sources within a radius of 15' and 10' around the field centre, respectively. The continuous, dashed, and dotted lines refer to detections in the soft, hard, and very hard bands; the straight line corresponds to the expected number of spurious detections based on the detection likelihood as defined in section 4.1 and assuming 20000 trials in the full

⁴ Changing the spectral index by $\Delta\Gamma=0.3$ would result in only a few percent difference in the number of the simulated sources at the limiting flux.

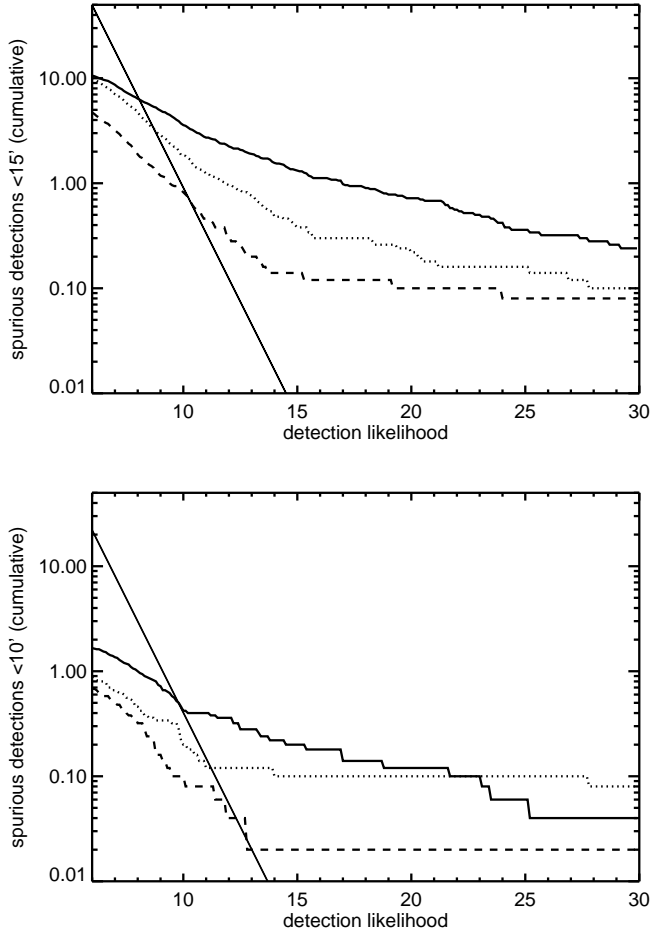


Fig. 4. Number of spurious detections from simulations as a function of likelihood. *Upper panel:* spurious detections within 15' around the field centre. *Lower panel:* the same as above but in the area of optical follow-up observations within 10' off the field centre. The soft, hard, and very hard energy bands are represented by solid, dashed, and dotted lines, respectively. The straight lines correspond to the expected number of spurious detections based on the detection likelihood as defined in section 4.1, assuming 20000 (upper panel) and 8900 (lower panel) independent detection cells in the field.

field and 8900 trials within a radius of 10' which roughly corresponds to the number of independent detection cells assuming a point spread function size of 13'' half energy width. The deviation of the results of the Monte Carlo simulations from the straight line can be understood in terms of the dual detection thresholds of our multi-step detection procedure as well as due to the simultaneous Maximum Likelihood fitting of source positions and fluxes, both of which result in a reduction of the effective number of independent trials. It can be seen that most spurious detections occur outside a radius of 10' where the mean point spread function begins to broaden and assumes an elongated shape. Based on the results of the Monte Carlo analysis, we therefore decided to restrict our source catalogue to sources with detection likelihoods above 10, corresponding to up to 4 expected spurious detections within a radius of 15' and less than one within the inner 10', the area used for optical follow-up work. We also derived, for each energy band, the sky coverage

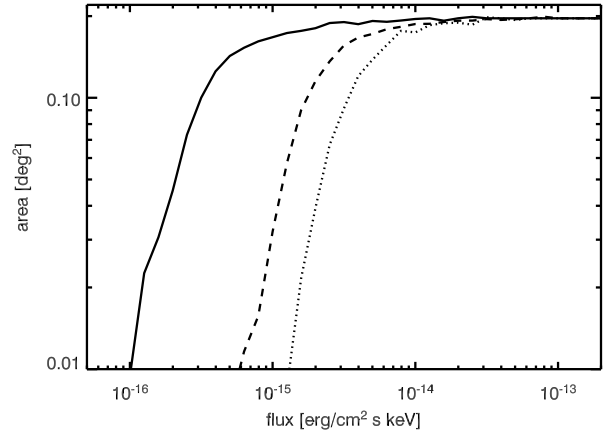


Fig. 5. Effective survey area as a function of detection sensitivity. The soft, hard, and very hard energy bands are represented by solid, dashed, and dotted lines, respectively.

as a function of the detection sensitivity, from the fraction of simulated input sources detected in each flux interval (Fig. 5).

4.3. Number counts

We computed the logN-logS relations in the soft, hard, and very hard energy bands using the sky coverage as determined from our Monte Carlo simulations (see Fig. 5) and by estimating the fluxes in the soft, hard, and very hard bands from the measured fluxes, assuming a power-law spectral index of $\Gamma = 1.4$. This spectral index was chosen for estimating the logN-logS fluxes to directly compare our source number counts to the results published in the literature. Most the deep X-ray surveys use this spectral index to model the spectra of the sources to match the spectral shape of the X-ray background. Changing the spectral index by $\Delta\Gamma \sim 0.3$ results in a flux change of <3% in the soft band and by <8% in the hard and very hard energy bands. Since the sky coverage was derived by realistic Monte Carlo simulations, distortions introduced by the presence of spurious sources in the catalogue are taken into account. In the same way we correct for the Eddington Bias.

Objects down to a detection likelihood of 6 in the respective energy band were considered for the determination of the number counts, corresponding to 5 to 10 expected spurious detections based on results from our Monte Carlo simulations (Fig. 4). If Ω_i is the sky coverage at a flux limit S_i , the cumulative number counts are obtained via:

$$N(> S_i) = \sum_{i=1}^{N_{\text{src}}} \frac{1}{\Omega_i}. \quad (1)$$

The logN-logS relations are plotted in Fig. 6, multiplied by $S^{1.5}$ in order to enhance deviations from the Euclidean behaviour. The logN-logS are compared with a sample of XMM-Newton, *Chandra*, ROSAT, and Beppo-Sax surveys.

We performed a Maximum Likelihood fit to the unbinned differential logN-logS. As commonly used in the literature, we assumed a broken power-law of the form

$$n(S) = \frac{dN}{ds} = \begin{cases} A S^{-\alpha_1} & S > S_b \\ B S^{-\alpha_2} & S \leq S_b, \end{cases} \quad (2)$$

Table 2. Best-fit parameters for logN-logS relation of eq. 2

energy band	A^a	α_1^b	S_b^c	α_2^d
0.5–2.0 keV	187	2.50*	1.23 ± 0.40	1.55 ± 0.05
2.0–10.0 keV	379	2.20 ± 0.16	0.88 ± 0.18	1.55 ± 0.12
5.0–10.0 keV	212	2.42 ± 0.18	0.53 ± 0.10	1.41 ± 0.34

^a Normalization in units of deg⁻² at 10⁻¹⁴ erg cm⁻² s⁻¹

^b Bright end slope

^c Cut-off flux in units of 10⁻¹⁴ erg cm⁻² s⁻¹

^d Faint end slope

* fixed

where $B = A S^{\alpha_2 - \alpha_1}$. α_2 and α_1 are the faint and bright slopes, respectively. S and the cut-off flux S_b are expressed in units of 10⁻¹⁴ erg cm⁻² s⁻¹ and A is the differential normalization in units of deg⁻² at 10⁻¹⁴ erg cm⁻² s⁻¹. The likelihood function \mathcal{L} , has been defined as in Murdoch, Crawford & Jauncey (1973). The best-fit parameters $\alpha_{1\text{best}}$, $\alpha_{2\text{best}}$ and $S_{b\text{best}}$ satisfy the condition $-2\mathcal{L}(\alpha_{1\text{best}}, \alpha_{2\text{best}}, S_{b\text{best}}) = \min$, the confidence intervals are defined to be $\Delta\mathcal{L} = \mathcal{L}(\alpha_1, \alpha_2, S_b) - \mathcal{L}_{\text{best}}$ where $\mathcal{L}_{\text{best}}$ is the minimum likelihood. Since \mathcal{L} is distributed like χ^2 , for 3 interesting parameters, the 1 σ confidence interval is $\Delta\mathcal{L}=3.53$. In the soft band because of the low statistics at the bright end of the logN-logS, we fixed α_1 to 2.50; the best-fit value of the free parameters are $\alpha_2=1.55 \pm 0.05$, $S_b=1.23 \pm 0.40 \times 10^{-14}$ erg cm⁻² s⁻¹ and $A=187$ deg⁻². In the hard band the best-fit parameters are $\alpha_1=2.20 \pm 0.16$, $\alpha_2=1.55 \pm 0.12$, $S_b=0.88 \pm 0.18 \times 10^{-14}$ erg cm⁻² s⁻¹ and $A=379$ deg⁻². In the very hard band we obtained $\alpha_1=2.42 \pm 0.18$, $\alpha_2=1.41 \pm 0.34$, $S_b=0.53 \pm 0.10 \times 10^{-14}$ erg cm⁻² s⁻¹ and $A=212$ deg⁻². The results of the fit are summarized in table 2. In order to visualize the results of the fits, in Fig. 6 we plotted the logN-logS relations and their best-fit broken power-laws and the data/model ratios in the lower panel. As can be noticed, the faint end part is well represented by our fits in all the energy bands. In the soft band, where the parameter α_1 was frozen, the fit underestimates the source number counts. This effect is caused by the well known overdensity of bright X-ray sources in the Lockman Hole resulting in a flattening of the relation at high fluxes. This effect is discussed in detail in Section 5. In the other energy bands our fits reproduce well the behaviour of the logN-logS relations also at the bright end side, though the bright end slopes remain slightly flatter than the canonical $\alpha_1=2.5$.

4.4. Source catalogue

In order to obtain a source catalogue which is largely free of spurious detections we limited the catalogue to objects with a full band detection likelihood > 10 , corresponding to up to 4 spurious detections based on our Monte Carlo simulations, which is $\sim 1\%$ of the detected objects. Table 3 lists the detection likelihoods, fluxes, and flux errors (1σ) in the total band, as well as in each of the three individual bands. The fluxes were calculated from the combined EPIC pn and MOS count rates determined by Maximum Likelihood fitting of the point spread function and assuming a power-law spectral index of $\Gamma = 2.0$. While source detection was performed in the three non-overlapping energy bands 0.5–2 keV, 2–4.5 keV, and 4.5–10 keV, source fluxes are quoted in the soft, hard, and very hard band (see Section 3) to better compare our data with published results. The total band fluxes were calculated by summing the soft and hard band fluxes. For a fraction of the sources significant detections

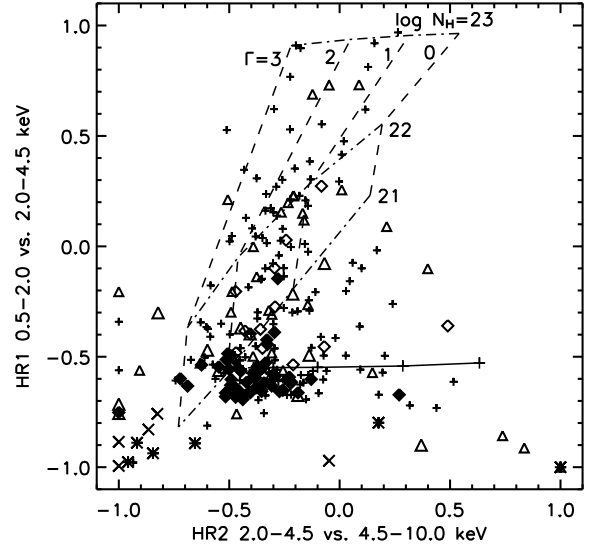


Fig. 7. X-ray colour-colour plot. Hardness ratios of objects with identified counterparts (filled diamonds: Type-I AGN, open diamonds: Type-II AGN, Open triangles: normal galaxies, crosses: clusters and groups, stars: stars) and for objects (+) where both hardness ratios have 1σ errors < 0.25 . Error bars were omitted for clarity; typical 1σ errors are in the range 0.05–0.25 (see table 3). Grid lines: location of objects with different absorbed power-law spectra. Dashed lines: location of objects with spectral index $\Gamma = 0$ to 3; Dot-dashed lines: photoelectric absorption levels from $\log(N_H)=21$ to $\log(N_H)=23$. Solid line: reflection+leaky absorber model, see text for details.

were only achieved in a subset of the energy bands. Individual band flux values with corresponding detection likelihood values of less than 10 should therefore not be regarded as significant detections. The flux errors are the statistical uncertainties estimated from the Maximum Likelihood and do not include uncertainties introduced by the choice of the spectral model to estimate the flux. In Section 4.3 we estimated the variation of the flux by changing the spectral index by $\Delta\Gamma=0.3$, this is $\sim 3\%$ in the soft band and $\sim 8\%$ in the hard and very hard bands. In total 340, 266, and 98 sources were detected in the soft, hard, and very hard band, respectively corresponding to a total of 409 unique sources. There are 117 sources which were only detected in the soft band and 37 sources only detected in the hard band. All of the 98 sources detected in the very hard band were also seen in the hard band. Six of the objects detected in the very hard band were sufficiently absorbed such that they were not visible in the soft band. We have assigned unique numbers⁵ to each of the detected sources. In the background subtracted full band image of Fig. 3 each detected source is marked by its 1σ positional error circle and source number. The ROSAT Lockman Hole catalogue (Lehmann et al. 2001) was searched for counterparts in the XMM-Newton catalogue. ROSAT sources falling within 6'' from the XMM-Newton centroid were identified as previously observed and their ROSAT source number is given. For most of these objects the ROSAT and XMM-Newton soft band fluxes were found to be broadly in agreement within statistical errors

⁵ The numbering scheme was chosen for internal, technical reasons; it does not reflect any of the tabulated source properties.

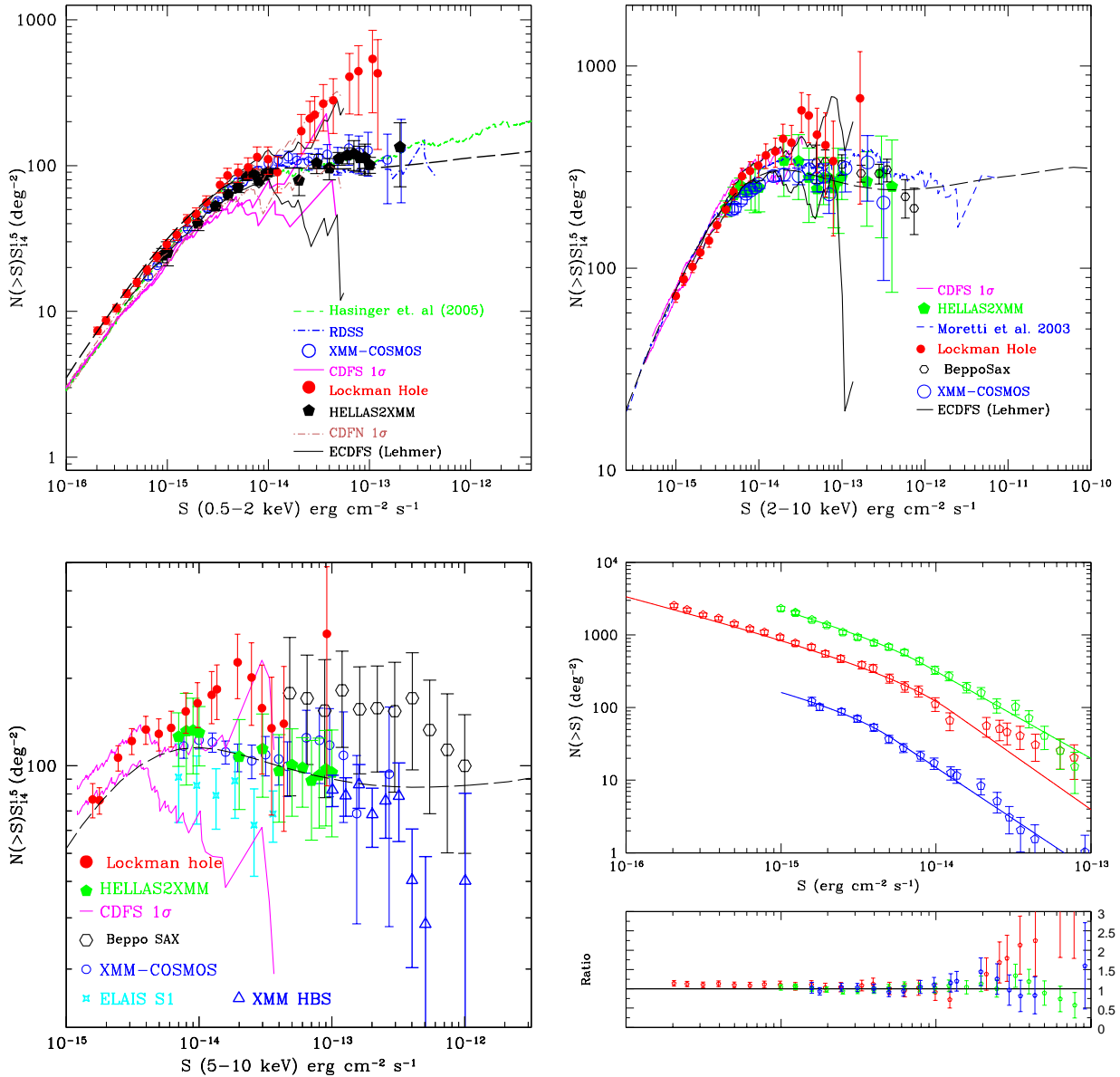


Fig. 6. logN-logS relations multiplied by $S^{1.5}$ in the 0.5–2.0 keV (top left), 2.0–4.5 keV (top right) and 4.5–10.0 keV (bottom left) energy bands. The data are compared to those obtained in the XMM-COSMOS survey (Cappelluti et al. 2007), the HELLAS2XMM survey (Baldi et al. 2002), the compilations of X-ray surveys produced by Moretti et al. (2003) and Hasinger et al. (2005), the Beppo-Sax survey (Fiore et al. 2001, Giommi et al. 2000), the *Chandra* deep surveys CDFN and CDFS (Rosati et al. 2002, Bauer et al. 2004), the RDSS (Hasinger et al. 1993), the extended CDFS (Lehmer et al. 2005), the ELAIS-S1 survey (Puccetti et al. 2006) and the XMM-HBS survey (Della Ceca et al. 2004). The black dashed lines represents the prediction of the X-ray background model of Gilli et al. (2007). Bottom left: in the upper panel the X-ray logN-logS in the Lockman Hole field (pentagons), and the broken power-law fits (solid lines) in the soft, hard, and very hard energy band, in red, green, and blue, respectively. For clarity the very hard band relation is divided by ten. In the lower panel data/model ratio, colour code as in the upper panel.

and considering the somewhat different spectral response of the instruments, with an indication for variability of up to a factor of ~ 2.5 in a subset of the objects.

We list two hardness ratios for each source, defined as

$$HR_1 = \frac{B_2 - B_1}{B_2 + B_1} \quad \text{and} \quad HR_2 = \frac{B_3 - B_2}{B_3 + B_2}$$

where B_1 , B_2 , and B_3 refer to the vignetting corrected count rates, summed over all three XMM-Newton cameras, in the soft,

hard, and very hard energy bands, respectively. Statistical 1σ hardness ratio errors were calculated from the count rate errors by error propagation. In Fig. 7 the hardness ratios are displayed in the form of an X-ray colour-colour plot. The plot contains 259 objects 125 of which have known spectroscopic classifications, both from optical follow-up of previous ROSAT observations (69 objects; Lehmann et al. 2001) and from the ongoing optical follow-up work of the XMM-Newton observations (Szokoly et al., in preparation). The remainder of the objects are as yet

unidentified XMM-Newton detections where the statistical 1σ error of both hardness ratios is less than 0.25 (134 objects). The objects with large hardness ratio errors are omitted for display purposes only; except for their larger scatter, we did not see any obvious deviation of the distribution of their X-ray colours from the displayed objects. Filled and open diamonds refer to Type-I and Type-II AGN, respectively. Galaxies are shown as open triangles, clusters and groups are displayed as crosses (X), and stars are shown as stars. The small plus signs correspond to as yet unidentified XMM-Newton objects. The grid lines refers to spectral models that were folded through the instrument response of the pn+MOS1+MOS2 detectors, using XSPEC. Each grid line corresponds to a simple power-law spectrum with photon indices $\Gamma = 0, 1, 2, 3$ (from right to left) and intrinsic absorption (in the observer frame) of $N_H = 10^{21}, 10^{22}$ and 10^{23} cm^{-2} (from bottom to top). While most Type-I AGN tightly cluster in one location consistent with a standard AGN-type power-law spectrum with very little absorption, Type-II AGN fill most of the HR_1 -range, corresponding to observer frame absorption up to 10^{23} cm^{-2} .

A small number of predominately Type-II AGN is found to have HR_1 hardness ratios typical of Type-I AGN but relatively hard corresponding HR_2 values, inconsistent with a single absorbed power-law. Our hypothesis is that these sources are Compton thick ($N_H > \sim 1.5 \times 10^{24} \text{ cm}^{-2}$) objects, whose spectrum is dominated by a Compton-reflection continuum from a cold medium which is usually assumed to be produced by the inner side of the putative obscured torus plus a soft power-law which is made by the photons "leaking" through the absorber. We used the XSPEC model "pexrav" (Magdziarz & Zdziarski 1995) to reproduce such a spectrum and to compute the expected hardness ratios. The track in Fig. 7 has been obtained for a leaking flux going from 1 to 30% of the total flux observed, from right to left. The increase of the leaking flux dilutes more and more the signature of the reflection component, modifying therefore the X-ray colours. The fraction of the flux due to reflection and leaking flux is described by the parameter "rel_refl" of the pexrav model. These objects may thus be representatives of a class of very highly absorbed AGN which due to the soft flux leaked through a partially covered absorber are detectable by XMM-Newton.

A source table giving the full details of the detection results is available in electronic form.

A separate source detection run was performed where sources were tested for significant extent beyond the size of the point spread function, assuming a King profile (see details in section 4.1). 13 objects were found with significant extent (likelihood of extent > 15 , corresponding to 5σ) with best-fit King profile extent values in the range from $1.5''$ to $20''$. Three objects where the best-fit extent reached the maximum permitted value of $20''$ were discarded as experience with the detection software shows that such objects tend to be spurious. In addition, two objects with extent sizes below $1''$ were assumed to be artifacts of inaccuracies in the modeling of the point spread function and were discarded from the list of extended objects. Table 4 lists the source positions, the likelihood of detection and likelihood of extent, and the best-fit King profile extent in arcsec, as well as source fluxes and hardness ratios. Where the detected extended objects overlapped with detections from our list of point sources, the source numbers from the point source list are given. Only one extended object was not also detected in our point source search. Of the seven ROSAT objects within the area covered by the current analysis, classified as either groups or clusters of galaxies, five were detected as extended by XMM-Newton. The remaining two objects appear pointlike on the XMM-Newton

image and were only detected as point sources. One object classified as Type-II AGN in Lehmann et al. (2001) was found to be marginally extended.

5. Discussion

It is known from the literature that the shape of the extragalactic X-ray logN-logS is well constrained (see e.g. Kim et al. 2006 and references therein). The normalizations of such relations show a wide field to field variation (see e.g. Cappelluti et. al 2005, 2007, Yang et al. 2003 and references therein). These fluctuations have been explained by superposition of Poissonian noise and fluctuations introduced by the clustering of the sources. The relative importance of these two components strongly depends on the depth and the sky coverage of the survey. In pencil beam surveys there is a higher chance of detecting strong variations, introduced at the bright end by the low count statistics and at the faint end by chance sampling of local large scale structures. In section 4.3 we presented the logN-logS relation for the X-ray sources in the XMM-Newton Lockman Hole survey in the context of previous results (see Fig. 6). In order to compare our results with previously published work we performed a comparison of the best-fit parameters together with a visual inspection of the plots.

- At fluxes lower than $10^{-14} \text{ erg cm}^{-2} \text{ s}^{-1}$, the soft band logN-logS relation shows an excellent agreement with previous surveys. Also, the best-fit parameters in this flux region are in agreement with results presented in previous surveys and summarized in Kim et al. (2006). As an example, the value of $\alpha_2=1.55\pm 0.05$ measured in this work is consistent within 1σ with the results of Hasinger et al. (2005) who obtained $\alpha_2=1.55\pm 0.04$, and with those of Moretti et al. (2003) who measured $\alpha_2=1.57\pm 0.10$. Both of the above cited works have been performed by merging the catalogues and the sky coverages of most of the *Chandra*, XMM-Newton and ROSAT surveys. Interestingly enough, at fluxes lower than S_b , our logN-logS is in good agreement also with the prediction of Gilli et al. (2007) based on X-ray background population synthesis. At the bright end of the distribution we detected an excess of sources. This is known to be a field selection effect of the Lockman Hole introduced to improve the ROSAT attitude precision (see e.g. Hasinger et al. 1998). Such an overdensity is however not statistically significant, and following Cappelluti et al. (2007), this can be explained by Poisson fluctuations in the low source surface density regime. Without considering the bright end excess it is worth noting that the normalization measured in this work is in excellent agreement with those measured in the XMM-COSMOS field which, being obtained on an area of $\sim 2 \text{ deg}^2$, can be considered as not affected by cosmic variance at a level $> 5\%$.
- In the hard band we were able to constrain all the parameters of the logN-logS and, even in this band, our results agree with most of the previous survey results listed in table 4 of Kim et al. (2006). Also in this band the best-fit parameters are in excellent agreement with those of the XMM-COSMOS survey with smaller errors on α_2 due to a better sampling of the flux interval below the knee of the relation. A direct comparison with the compilation of Moretti et al. (2003) who obtained $\alpha_2=1.44\pm 0.13$ also shows a 1σ consistency. The bright end slope, $\alpha_1=2.2\pm 0.12$ measured in this work is somewhat flatter than the expected Euclidean 2.5. This can be explained with the overdensity of bright sources at the bright end as observed in the soft band.

- In the 5–10 keV band the flux range of the XMM-Lockman Hole survey allows us to sample with very good statistics the regions above and below S_b . The position of the break is in good agreement with the predictions of Gilli et al. (2007). We were able, for the first time, to constrain α_2 in this band but with quite large uncertainty. The normalization shows a ~40% higher value than in the XMM-COSMOS survey. This band is in fact more sensitive to the bright source overdensity. Since all the bright sources in the soft band source excess are detected in the very hard band, the fraction of bright sources which reside in the source excess is higher in this band than in the soft and hard energy bands. A consequence of this peculiarity is therefore an increase of the normalization of the logN-logS along the totality of the relation. At the very faint end in fact the overdensity gets weaker. The points of the logN-logS are in agreement with the measurement of the CDFS, HELLAS2XMM and partly with the X-ray background model of Gilli et al. (2007). Moreover, with the only exception of the CDFS, whose points are in agreement with ours below the knee, all the surveys derive their fluxes using $\Gamma=1.7$ as model spectral index. This has the effect of reducing the normalization, in this band, by ~15%.

The contribution of the Lockman Hole X-ray sources to the X-ray background has been discussed in detail by Worlsey et al. (2005) resulting in important conclusions on the nature of the missing sources of the X-ray background. The distribution of the different types of sources contributing to the X-ray background can, in the first instance, be determined by carefully examining the colour-colour diagram. Type-I AGN are clustered in a well defined region, corresponding to low intrinsic absorption and photon indices in the range 1.7–2 as determined by Mainieri et al. (2002). The bulk of the distribution of Type-I AGN, seems to be right-shifted from the no absorption locus, suggesting the presence of additional spectral components. On the other hand, Type-II AGN show higher hardness ratios, corresponding to higher intrinsic absorption. As pointed out by Hasinger et al. (2007) in the COSMOS field, there is evidence of candidate Type-II AGN with quite hard colours in the hard bands (HR_2), and soft band colours (HR_1) consistent with unabsorbed sources. The solid horizontal line in Fig. 7 shows however that their colours are similar to those of heavily absorbed sources at low redshift, with a small fraction of unabsorbed flux leaking out.

At higher redshift the absorbed continuum moves to softer energy and therefore the source shifts to another locus on the colour-colour plot. A single prototype of these objects has been detected in the Lockman Hole by Mainieri et al. (2002). The source #290 (ROSAT #901), at redshift $z=0.204$, shows an absorbed power-law hard component with $N_{\mathrm{H}} \sim 5 \times 10^{23} \text{ cm}^{-2}$ and an additional soft steep $\Gamma \sim 3$ unabsorbed component. A similar result could be obtained also with the “pexrav” XSPEC model. Mateos et al. (2005) detected sources with high absorption and evidence of soft excess. First results from the XMM-COSMOS survey (Hasinger et al. 2007, Mainieri et al. 2007) pointed out that this kind of source could be among the most highly absorbed objects detectable in an X-ray survey. Selecting sources with $HR_1 < -0.1$, $HR_2 > 0.1$ and errors in both hardness ratios less than 0.25, we obtained a sample of 13 candidate Compton thick sources, corresponding to a fraction of ~6% of Compton thick objects. The faintest among these sources has a 2–10 keV flux of $\sim 9 \times 10^{-16} \text{ erg cm}^{-2} \text{ s}^{-1}$. In the *Chandra* deep field Tozzi et al. (2006) spectroscopically detected 14/280 candidates at 2–10 keV fluxes greater than $\sim 1.5 \times 10^{-15} \text{ erg cm}^{-2}$

s^{-1} . Polletta et al. (2006), detected 5/567 X-ray selected candidates in the *Chandra* SWIRE survey at 2–10 keV fluxes greater than $\sim 4.6 \times 10^{-15} \text{ erg cm}^{-2} \text{ s}^{-1}$. In the XMM-COSMOS survey Hasinger et al. (2007) selected in the same way as in this paper 18/600 candidates with fluxes greater than $\sim 3.3 \times 10^{-15} \text{ erg cm}^{-2} \text{ s}^{-1}$. In the lower panel of Fig. 8 we plot the fraction of Compton thick candidates as a function of the flux of the deepest candidate sources in the surveys mentioned above.

We note that this determination is in good agreement with X-ray background model predictions (see e.g. Fig. 16 in Gilli et al. 2007). Indeed, the fraction of Compton thick sources shows a growth of a factor ~5 in the 2–10 keV flux interval $\sim 4.6 \times 10^{-15} \text{ erg cm}^{-2} \text{ s}^{-1}$ to $\sim 9 \times 10^{-16} \text{ erg cm}^{-2} \text{ s}^{-1}$. In order to obtain the first measurement of the surface density of Compton thick sources, we multiplied the source fraction estimated above in the 2–10 keV band by the cumulative number density predicted by Gilli et al. (2007). The resulting logN-logS is shown in the upper panel of Fig. 8. Such a logN-logS is well represented by a single power-law of the form

$$N(> S) = 2.19 \pm 0.88 \times \left(\frac{S}{10^{14} \text{ erg cm}^{-2} \text{ s}^{-1}} \right)^{1.83 \pm 0.23} \text{ deg}^{-2} \quad (3)$$

We therefore conclude that the number density of Compton thick sources in deep XMM-Newton and *Chandra* surveys is rising according to an Euclidean growth. The observed growth of the fraction of Compton thick sources at low fluxes is in good agreement with models. Such a relation, if confirmed at fainter fluxes would, in principle, explain the observed shape and the position of the peak of the X-ray background spectrum.

6. Conclusion

We analyzed a set of 18 XMM-Newton pointings centred on the Lockman Hole which constitute the deepest exposure performed by XMM-Newton, reaching a sensitivity limit of $1.9 \times 10^{-16} \text{ erg cm}^{-2} \text{ s}^{-1}$, $9 \times 10^{-16} \text{ erg cm}^{-2} \text{ s}^{-1}$ and $1.8 \times 10^{-15} \text{ erg cm}^{-2} \text{ s}^{-1}$, in the 0.5–2.0 keV, 2.0–10.0 keV and 5.0–10.0 keV energy bands, respectively. 409 sources were detected within the survey area of 0.20 sq. degrees. 340, 266, and 98 objects were detected in the soft, hard, and very hard band, respectively. A catalogue including the main X-ray characteristics of the sources in the Lockman hole survey is presented. The number counts derived from the XMM-Newton data are in close agreements with previous surveys and the most recent synthesis models of the X-ray background. Differences in the normalization of our logN-logS with those of other surveys have been discussed and explained in terms of low counting statistics typical of deep pencil beam surveys. The high throughput of the XMM-Newton telescope allowed us to compute and constrain the parameters of the logN-logS in the hard and very hard energy bands. This region of the X-ray spectrum is fundamental for understanding absorbed AGNs which are thought to be the most important contributors to the total flux of the X-ray background. We also present the colour-colour diagram for our X-ray sources, which confirms, together with the spectral analysis on this field performed by Mateos et al. (2005) and Mainieri et al. (2002), the presence of a conspicuous number of highly absorbed AGNs together with evidence of the increasing fraction of this kind of objects at low X-ray fluxes.

Acknowledgements. In Germany the XMM-Newton project is supported by the Bundesministerium für Bildung und Forschung/Deutsches Zentrum für Luft und Raumfahrt and the Max Planck Society. Part of this work was supported by the DLR project numbers 50 OR 0207 and 50 OR 0405. XB acknowledges support

Table 3. Catalogue of X-ray sources with likelihood of detection in 0.5–10 keV band greater than 10 (3.9 σ). Description of columns: (1) XMM-Newton source number as displayed in Fig. 3, (2) ROSAT source number (Lehmann et al. 2001), (3) IAU source name, (4–6) J2000 coordinates and errors, (7–18) likelihood of detection (rounded to nearest integer), fluxes and flux errors [10^{-16} erg cm $^{-2}$ s $^{-1}$] in 0.5–10, 0.5–2, 2–10, and 5–10 keV band, (19–22) hardness ratios and errors (see text for band definitions). All errors are 1 σ errors.

SRC # XMM R	IAU name	RA	DEC	err	0.5–10.0 keV			0.5–2.0 keV			2.0–10.0 keV			5.0–10.0 keV			HR1	err	HR2	err	
		hh mm ss	° ' "		\mathcal{L}	flux	err	\mathcal{L}	flux	err	\mathcal{L}	flux	err	\mathcal{L}	flux	err					
352	XMMU J105053.0+573028	10 50 53.05	57 30 28.5	2.4	13	21.0	6.1	12	5.6	1.2	3	15.4	6.0	0	2.6	7.6	-0.39	0.19	-0.79	0.56	
358	17	XMMU J105104.0+573053	10 51 4.04	57 30 53.8	0.3	2242	233.4	8.7	1896	87.1	2.3	311	146.3	8.4	37	111.7	15.0	-0.58	0.02	-0.30	0.07
458		XMMU J105106.4+573435	10 51 6.46	57 34 35.6	0.4	744	238.9	10.7	134	18.6	1.5	492	220.3	10.6	118	239.6	20.0	0.30	0.04	-0.13	0.05
430	11	XMMU J105108.3+573345	10 51 8.38	57 33 45.4	0.2	3406	363.1	10.4	2522	102.0	2.4	792	261.1	10.2	92	186.7	16.9	-0.42	0.02	-0.33	0.04
1522		XMMU J105108.4+572833	10 51 8.46	57 28 33.6	1.7	15	18.9	4.3	0	0.0	0.5	11	18.9	4.3	5	33.9	10.1	1.00	0.30	0.12	0.19
500		XMMU J105108.9+573553	10 51 8.97	57 35 53.0	1.0	78	62.0	8.1	40	11.1	1.4	28	51.0	8.0	10	79.1	18.5	-0.16	0.10	0.05	0.14
217		XMMU J105111.8+572635	10 51 11.87	57 26 35.4	0.2	1816	160.1	6.5	1531	57.1	1.6	270	103.0	6.3	17	56.9	10.6	-0.56	0.02	-0.44	0.08
357		XMMU J105112.8+573035	10 51 12.87	57 30 35.7	1.4	20	18.8	4.1	14	4.1	0.8	7	14.7	4.0	0	9.1	9.4	-0.28	0.16	-0.39	0.45
1361		XMMU J105114.8+573551	10 51 14.86	57 35 51.4	1.2	31	37.1	6.1	0	0.6	0.8	23	36.5	6.1	10	67.1	15.5	0.81	0.22	0.13	0.14
1489		XMMU J105116.0+572015	10 51 16.03	57 20 15.2	1.7	10	25.1	7.0	4	3.7	1.2	5	21.4	6.8	1	30.6	15.7	-0.05	0.23	0.01	0.30
1417		XMMU J105116.8+572109	10 51 16.82	57 21 9.8	0.9	32	35.2	5.9	15	5.6	1.1	16	29.5	5.8	1	25.2	13.5	-0.09	0.14	-0.25	0.27
41	46	XMMU J105120.0+571848	10 51 20.10	57 18 48.9	0.4	415	117.5	10.2	370	45.7	2.4	38	71.8	9.9	7	78.5	20.9	-0.60	0.05	-0.13	0.15
202		XMMU J105120.4+572603	10 51 20.49	57 26 3.7	0.7	131	36.2	4.3	106	10.9	0.9	25	25.3	4.1	2	19.5	8.7	-0.46	0.07	-0.29	0.22
226		XMMU J105120.6+572701	10 51 20.66	57 27 1.7	0.3	973	96.7	5.3	834	35.4	1.3	127	61.3	5.1	14	44.8	9.1	-0.57	0.03	-0.32	0.10
2134		XMMU J105120.7+572515	10 51 20.74	57 25 15.2	1.0	23	26.5	4.4	12	5.5	0.9	10	21.0	4.3	1	22.5	8.9	-0.24	0.13	-0.14	0.22
174		XMMU J105120.8+572458	10 51 20.82	57 24 58.5	0.5	23	60.9	5.3	12	21.9	1.3	10	39.0	5.2	1	21.0	10.3	-0.56	0.05	-0.45	0.20
1395		XMMU J105121.2+571938	10 51 21.21	57 19 38.3	2.9	13	22.7	6.8	12	6.3	1.4	2	16.4	6.7	0	19.8	16.3	-0.42	0.19	-0.08	0.46
313		XMMU J105121.2+572932	10 51 21.25	57 29 32.5	1.0	41	31.6	4.4	1	1.1	0.6	38	30.5	4.4	3	23.4	8.8	0.62	0.17	-0.30	0.18
111		XMMU J105122.3+572214	10 51 22.30	57 22 14.6	0.6	122	35.0	4.9	111	12.8	1.1	13	22.2	4.7	0	12.3	10.7	-0.57	0.08	-0.44	0.36
530		XMMU J105122.6+573734	10 51 22.63	57 37 34.7	1.3	21	28.5	6.1	14	6.0	1.2	8	22.5	6.0	0	11.6	13.2	-0.25	0.16	-0.47	0.46
89		XMMU J105123.3+572048	10 51 23.34	57 20 48.1	0.7	85	55.9	6.4	0	0.4	0.6	57	55.5	6.4	30	108.0	15.9	0.92	0.13	0.16	0.09
1458		XMMU J105125.2+572903	10 51 25.28	57 29 3.8	2.5	100	14.1	3.5	7	0.6	0.5	1	13.5	3.5	0	28.5	7.6	0.56	0.32	0.20	0.18
354	75	XMMU J105125.4+573050	10 51 25.40	57 30 50.7	0.2	2206	154.3	6.0	1873	58.4	1.6	294	95.9	5.8	41	74.5	9.8	-0.59	0.02	-0.29	0.07
490		XMMU J105125.4+573542	10 51 25.45	57 35 43.0	1.1	63	17.9	4.5	65	11.4	1.2	0	6.5	4.3	0	11.5	11.6	-0.83	0.10	0.11	0.59
109		XMMU J105126.2+572208	10 51 26.24	57 22 8.1	0.8	90	20.9	4.1	91	11.0	1.0	2	9.9	4.0	0	0.9	5.6	-0.75	0.09	-0.87	0.70
474		XMMU J105128.2+573502	10 51 28.20	57 35 2.5	0.4	816	88.1	5.6	772	46.9	1.8	45	41.2	5.4	2	28.6	11.3	-0.76	0.03	-0.34	0.18
243		XMMU J105128.2+572740	10 51 28.23	57 27 40.1	0.2	3042	308.8	8.2	1126	40.4	1.3	1618	268.4	8.1	299	220.0	12.5	0.03	0.02	-0.27	0.03
2342		XMMU J105128.7+572856	10 51 28.78	57 28 56.1	1.4	11	15.3	3.3	0	0.0	0.2	12	15.3	3.3	1	15.5	7.3	1.00	0.16	-0.17	0.25
280		XMMU J105128.9+572823	10 51 28.96	57 28 23.0	1.5	11	7.6	3.0	12	3.0	0.6	0	4.6	2.9	0	2.7	4.8	-0.61	0.21	-0.41	0.78
523		XMMU J105129.9+573736	10 51 29.93	57 37 36.9	0.2	1550	188.3	8.4	1346	73.4	2.2	189	114.9	8.1	16	85.1	16.2	-0.60	0.02	-0.31	0.09
112		XMMU J105130.5+572220	10 51 30.50	57 22 20.3	0.5	162	14.4	3.4	167	14.4	1.0	0	0.0	3.2	0	1.3	4.9	-1.00	0.07	1.00	7.18
235		XMMU J105130.8+572705	10 51 30.89	57 27 5.7	1.4	27	22.0	3.7	5	2.1	0.6	20	20.0	3.6	2	17.9	7.1	0.21	0.17	-0.22	0.21
444	8	XMMU J105131.0+573440	10 51 31.01	57 34 40.0	0.1	82940	1457.9	12.5	80900	1071.2	6.4	1987	386.6	10.7	56	114.1	12.8	-0.89	0.00	-0.66	0.03
1405		XMMU J105131.4+571928	10 51 31.45	57 19 28.9	1.3	24	25.3	5.6	19	6.2	1.1	6	19.1	5.5	0	15.6	14.0	-0.34	0.15	-0.27	0.44
213		XMMU J105132.0+572616	10 51 32.02	57 26 18.7	0.6	183	37.9	3.9	140	11.3	0.9	35	26.7	3.8	8	32.9	8.3	-0.45	0.06	-0.07	0.14
160		XMMU J105132.3+572414	10 51 32.35	57 24 14.1	1.5	31	18.5	3.6	24	4.4	0.7	9	14.1	3.5	0	7.7	7.7	-0.32	0.13	-0.44	0.41
2506		XMMU J105133.7+573525	10 51 33.75	57 35 25.9	2.0	100	13.3	4.0	7	3.1	1.0	5	10.1	3.9	1	13.1	9.2	-0.32	0.22	-0.05	0.40
578		XMMU J105134.9+574019	10 51 34.95	57 40 19.8	1.7	16	47.2	9.1	0	0.4	0.9	16	46.8	9.1	2	46.4	21.0	0.90	0.21	-0.18	0.24
248		XMMU J105135.7+572740	10 51 35.72	57 27 40.4	0.9	99	37.8	3.9	24	4.0	0.6	62	33.8	3.8	14	34.2	7.0	0.15	0.10	-0.17	0.11
2507		XMMU J105135.7+573521	10 51 35.75	57 35 21.9	2.0	100	2.4	2.0	3	1.9	0.9	0	0.5	1.8	0	0.0	1.8	-0.92	0.28	-1.00	5.08
99		XMMU J105136.0+572135	10 51 36.04	57 21 35.6	0.6	156	52.6	5.0	87	10.2	1.0	59	42.3	4.9	11	48.1	10.8	-0.21	0.07	-0.11	0.12
415		XMMU J105136.3+573303	10 51 36.33	57 33 3.6	0.7	129	29.1	3.6	109	9.8	0.8	20	19.3	3.5	1	14.0	7.3	-0.52	0.07	-0.32	0.25
437		XMMU J105136.4+573333	10 51 36.50	57 33 33.4	1.4	18	19.5	3.7	3	1.8	0.7	15	17.7	3.6	1	13.4	7.8	0.23	0.20	-0.31	0.28
316		XMMU J105136.9+572940	10 51 37.00	57 29 40.8	0.9	57	20.7	3.2	43	5.4	0.7	15	15.3	3.1	0	5.5	5.8	-0.38	0.10	-0.59	0.35
295	837	XMMU J105137.1+572857	10 51 37.18	57 28 57.8	0.6	114	19.4	3.2	102	8.7	0.8	6	10.8	3.1	7	26.5	6.9	-0.67	0.08	0.27	0.18
529		XMMU J105137.3+573755	10 51 37.38	57 37 56.0	0.2	3616	357.3	10.7	2910	118.3	2.7	634	238.9	10.4	74	184.7	18.6	-0.52	0.02	-0.29	0.05
353	19	XMMU J105137.3+573043	10 51 37.38	57 30 43.6	0.3	1063	93.4	4.6	853	29.8	1.1	202	63.7	4.5	10	30.9	7.3	-0.49	0.03	-0.49	0.09
212		XMMU J105139.2+572615	10 51 39.21	57 26 15.5	2.2	11	6.9	2.9	11	2.6	0.6	0	4.2	2.8	1	11.5	6.5	-0.60			

SRC # XMM	R	IAU name	RA (J2000)		DEC		err "	0.5–10.0 keV			0.5–2.0 keV			2.0–10.0 keV			5.0–10.0 keV			HR1	err	HR2	err
			hh mm ss	° ′ ″				flux	err		flux	err		flux	err		flux	err					
2366		XMMU J105145.3+573215	10 51 45.36	57 32 15.7	1.5	13	12.9	3.0	0	0.1	0.3	10	12.8	3.0	4	20.4	6.8	0.93	0.26	0.06	0.20		
426		XMMU J105145.3+573307	10 51 45.36	57 33 7.2	1.3	22	8.9	2.8	23	4.0	0.7	1	4.8	2.8	0	7.9	6.6	-0.68	0.16	0.07	0.50		
372		XMMU J105146.2+573110	10 51 46.25	57 31 11.0	0.9	35	20.3	3.1	0	0.6	0.5	29	19.7	3.1	7	21.8	6.0	0.69	0.22	-0.12	0.16		
351		XMMU J105146.5+573036	10 51 46.57	57 30 36.6	0.4	462	38.4	3.2	430	18.0	0.9	32	20.4	3.1	2	13.3	5.5	-0.70	0.04	-0.37	0.19		
16		XMMU J105146.9+571715	10 51 46.97	57 17 15.0	0.5	118	50.8	6.9	98	16.2	1.5	17	34.6	6.7	4	51.9	16.4	-0.50	0.08	0.03	0.19		
1572		XMMU J105147.4+571840	10 51 47.50	57 18 40.6	1.3	14	24.8	5.2	2	2.3	0.9	11	22.6	5.1	1	26.1	12.8	0.22	0.22	-0.10	0.27		
565		XMMU J105148.6+573932	10 51 48.63	57 39 32.9	0.5	152	59.2	6.3	112	16.4	1.4	34	42.8	6.1	6	58.4	16.2	-0.42	0.07	-0.02	0.16		
407	12	XMMU J105148.8+573248	10 51 48.85	57 32 48.4	0.1	5104	375.6	8.3	1845	48.9	1.3	2634	326.7	8.2	626	282.3	12.2	0.03	0.02	-0.24	0.02		
391		XMMU J105149.1+573153	10 51 49.13	57 31 53.7	2.1	10	3.3	1.6	11	2.5	0.6	0	0.8	1.5	0	7.2	5.4	-0.90	0.18	0.72	0.48		
1396		XMMU J105149.1+572858	10 51 49.16	57 28 58.9	1.0	38	8.9	2.4	39	4.3	0.6	1	4.6	2.4	0	0.0	4.5	-0.71	0.13	-1.00	1.37		
186		XMMU J105150.0+572521	10 51 50.10	57 25 21.6	0.2	2842	232.1	6.7	1462	40.1	1.2	1208	192.0	6.6	173	123.5	9.1	-0.14	0.02	-0.38	0.03		
395		XMMU J105151.4+573219	10 51 51.48	57 32 19.9	1.4	59	12.8	2.7	58	6.6	0.7	2	6.3	2.6	0	5.5	4.7	-0.74	0.10	-0.24	0.45		
555		XMMU J105152.1+573906	10 51 52.16	57 39 6.2	0.3	813	127.4	7.2	680	43.3	1.8	131	84.0	7.0	5	43.0	13.5	-0.53	0.03	-0.47	0.13		
1566		XMMU J105152.2+574104	10 51 52.28	57 41 4.5	1.6	20	17.5	5.8	17	7.0	1.3	1	10.6	5.7	3	46.8	17.8	-0.61	0.18	0.52	0.24		
492		XMMU J105153.7+573555	10 51 53.73	57 35 55.6	0.6	157	59.4	5.2	11	3.2	0.7	105	56.3	5.1	41	82.8	10.7	0.48	0.09	0.02	0.08		
57		XMMU J105154.1+571924	10 51 54.16	57 19 24.7	1.0	53	22.2	4.2	43	7.1	0.9	7	15.1	4.1	4	32.4	10.5	-0.50	0.11	0.20	0.20		
456	9	XMMU J105154.5+573437	10 51 54.50	57 34 37.6	0.1	5850	254.9	6.7	5102	104.5	1.9	701	150.4	6.4	48	72.3	8.9	-0.63	0.01	-0.49	0.05		
255		XMMU J105154.5+572751	10 51 54.54	57 27 51.7	0.9	40	16.9	2.7	23	3.2	0.5	15	13.7	2.7	2	7.5	4.6	-0.20	0.12	-0.44	0.26		
156		XMMU J105154.7+572407	10 51 54.71	57 24 7.4	0.4	584	59.4	3.9	487	19.7	0.9	94	39.7	3.8	5	21.3	6.4	-0.52	0.04	-0.45	0.13		
312		XMMU J105155.2+572932	10 51 55.27	57 29 32.6	0.5	178	25.9	3.0	157	10.1	0.8	20	15.8	2.9	2	13.3	5.7	-0.60	0.06	-0.26	0.22		
180		XMMU J105155.3+572458	10 51 55.38	57 24 58.2	0.4	222	31.2	3.3	196	11.5	0.8	27	19.7	3.2	0	8.7	5.8	-0.57	0.06	-0.52	0.25		
359		XMMU J105155.3+573043	10 51 55.39	57 30 43.4	0.7	198	31.5	3.0	154	9.3	0.7	43	22.2	3.0	3	14.1	5.3	-0.45	0.06	-0.38	0.17		
274		XMMU J105155.8+572812	10 51 55.82	57 28 12.0	1.5	20	11.5	2.5	7	1.9	0.5	9	9.6	2.4	5	16.6	5.0	-0.10	0.18	0.10	0.19		
436		XMMU J105156.4+573331	10 51 56.43	57 33 31.3	1.6	21	17.2	3.1	0	0.8	0.5	19	16.4	3.0	2	14.8	5.9	0.53	0.23	-0.22	0.21		
541		XMMU J105156.4+573802	10 51 56.44	57 38 2.2	1.3	15	13.9	3.9	12	3.7	0.8	3	10.2	3.8	0	16.0	9.8	-0.39	0.18	0.05	0.36		
61		XMMU J105157.6+571940	10 51 57.66	57 19 40.7	0.5	112	53.9	5.2	25	5.1	0.8	75	48.8	5.1	13	50.6	10.6	0.21	0.09	-0.16	0.11		
256		XMMU J105158.7+572758	10 51 58.79	57 27 59.0	1.3	28	16.9	2.7	6	1.7	0.5	21	15.2	2.7	2	10.7	4.8	0.16	0.16	-0.34	0.22		
405		XMMU J105158.8+573229	10 51 58.80	57 32 30.0	0.7	151	22.2	3.0	139	9.8	0.8	11	12.4	2.9	2	14.5	5.7	-0.67	0.07	-0.10	0.23		
163	33	XMMU J105200.1+572423	10 52 0.11	57 24 23.5	0.4	523	60.1	3.9	397	17.5	0.9	113	42.6	3.8	13	30.6	6.5	-0.44	0.04	-0.33	0.10		
31		XMMU J105200.4+571806	10 52 0.41	57 18 6.2	0.5	258	103.2	6.9	71	10.7	1.1	173	92.4	6.9	14	70.5	14.0	0.15	0.06	-0.30	0.10		
439		XMMU J105201.5+573337	10 52 1.58	57 33 37.4	1.1	15	14.1	3.0	3	1.5	0.5	11	12.6	3.0	1	12.1	6.3	0.16	0.21	-0.19	0.27		
77		XMMU J105201.6+572017	10 52 1.68	57 20 17.6	0.6	96	26.0	3.8	85	8.9	0.9	13	17.1	3.7	0	5.8	6.9	-0.53	0.08	-0.61	0.38		
512		XMMU J105202.2+573647	10 52 2.22	57 36 47.8	1.3	41	10.3	3.1	43	6.1	0.8	0	4.3	3.0	0	8.7	7.5	-0.80	0.13	0.18	0.54		
2278		XMMU J105203.8+572708	10 52 3.86	57 27 8.7	1.2	19	12.6	2.5	0	0.3	0.4	15	12.3	2.5	5	17.4	4.9	0.73	0.28	-0.00	0.17		
471		XMMU J105203.8+573500	10 52 3.87	57 35 0.1	1.2	22	12.8	3.1	11	2.7	0.6	6	10.1	3.0	5	23.3	7.0	-0.26	0.17	0.24	0.20		
142		XMMU J105203.9+572338	10 52 4.00	57 23 38.9	0.5	277	37.4	3.4	234	12.4	0.8	45	25.1	3.3	0	6.9	5.6	-0.51	0.05	-0.67	0.23		
2045		XMMU J105204.3+574108	10 52 4.35	57 41 8.7	0.3	206	210.2	11.2	190	81.6	3.1	16	128.6	10.7	1	51.0	18.3	-0.60	0.03	-0.56	0.13		
30		XMMU J105204.8+571806	10 52 4.87	57 18 6.7	0.7	92	38.2	5.2	64	9.7	1.0	21	28.5	5.0	7	48.5	12.7	-0.36	0.09	0.09	0.16		
568		XMMU J105205.2+573946	10 52 5.23	57 39 46.9	1.0	51	40.9	5.5	20	5.4	1.0	30	35.4	5.4	1	25.3	12.1	0.01	0.12	-0.33	0.22		
576		XMMU J105205.4+574014	10 52 5.42	57 40 14.5	1.0	79	33.1	5.6	69	11.9	1.2	8	21.3	5.4	3	36.4	13.4	-0.56	0.09	0.09	0.22		
233		XMMU J105205.4+572659	10 52 5.46	57 26 59.2	1.3	16	11.7	2.5	0	0.8	0.4	11	10.9	2.5	5	18.2	5.3	0.34	0.25	0.08	0.18		
584		XMMU J105206.1+574124	10 52 6.19	57 41 24.2	0.2	434	259.4	11.3	379	112.8	3.3	55	146.6	10.8	3	87.8	19.5	-0.66	0.02	-0.41	0.10		
411	53	XMMU J105206.2+571525	10 52 6.24	57 15 25.9	0.5	958	500.4	23.7	496	86.2	4.3	411	414.2	23.3	51	350.2	43.4	-0.14	0.04	-0.25	0.06		
126		XMMU J105206.4+572301	10 52 6.46	57 23 1.2	1.0	28	17.7	3.0	3	1.5	0.5	20	16.3	2.9	5	19.6	6.2	0.27	0.19	-0.08	0.18		
2046		XMMU J105206.5+574109	10 52 6.51	57 41 9.5	0.5	206	106.5	9.0	190	42.6	2.4	17	63.9	8.7	1	47.0	17.5	-0.62	0.05	-0.32	0.18		
110	825	XMMU J105206.5+572213	10 52 6.51	57 22 14.0	0.4	275	42.4	3.7	224	12.9	0.8	53	29.5	3.6	0	10.5	6.4	-0.47	0.05	-0.60	0.20		
306		XMMU J105206.8+572924	10 52 6.81	57 29 24.3	0.3	835	89.2	4.0	327	12.2	0.7	451	76.9	3.9	58	47.8	5.5	-0.00	0.04	-0.39	0.05		
522		XMMU J105207.0+573731	10 52 7.06	57 37 31.7	1.0	35	16.7	3.6	29	5.3	0.8	5	11.4	3.5	1	17.5	8.3	-0.49	0.13	0.04	0.28		
548	832	XMMU J105207.4+573838	10 52 7.44	57 38 38.3	0.4	374	57.3	5.0	339	22.2	1.2	37	35.1	4.9	0	8.1	8.8	-0.60	0.05	-0.72	0.27		
51		XMMU																					

SRC #	XMM	RA (J2000)	DEC	err	0.5–10.0 keV			0.5–2.0 keV			2.0–10.0 keV			5.0–10.0 keV			HR1	err	HR2	err	
					R	hh mm ss	° ′ ″	° ′ ″	flux	err	flux	err	flux	err	flux	err					
1591	XMMU J105212.6+572452	10 52 12.70	57 24 52.6	1.3	15	4.3	1.8		17	2.7	0.5	0	1.6	1.8	0	2.8	3.7	-0.82	0.18	0.10	0.84
307	XMMU J105212.9+572919	10 52 12.99	57 29 19.7	0.9	64	21.5	2.6	0	0.2	0.3	54	21.4	2.6	12	20.3	4.5	0.91	0.14	-0.20	0.12	
400	13	XMMU J105213.3+573221	10 52 13.35	57 32 21.2	0.2	3273	134.4	4.5	2818	52.4	1.2	423	82.0	4.3	34	39.7	5.7	-0.60	0.02	-0.49	0.06
201		XMMU J105213.6+572559	10 52 13.63	57 25 59.1	0.6	141	24.7	2.6	103	6.4	0.6	39	18.3	2.5	0	6.5	4.2	-0.37	0.07	-0.60	0.21
386		XMMU J105214.0+573140	10 52 14.06	57 31 40.6	0.9	46	19.0	2.7	8	1.7	0.4	32	17.3	2.6	6	16.1	4.3	0.23	0.14	-0.21	0.15
588		XMMU J105216.2+574108	10 52 16.27	57 41 8.6	0.4	263	79.6	7.3	220	25.3	1.7	44	54.3	7.1	1	27.4	14.7	-0.49	0.06	-0.47	0.21
566		XMMU J105216.5+573946	10 52 16.50	57 39 46.5	1.3	27	24.3	4.8	15	4.7	0.9	10	19.6	4.7	2	29.5	11.4	-0.20	0.15	0.03	0.23
526		XMMU J105216.6+573721	10 52 16.68	57 37 21.3	1.5	11	6.2	2.8	12	3.1	0.7	0	3.0	2.7	0	1.7	4.3	-0.73	0.21	-0.43	1.10
72		XMMU J105216.9+572018	10 52 16.95	57 20 18.0	0.2	4957	407.6	9.3	2383	65.9	1.6	2215	341.8	9.2	360	263.9	14.2	-0.10	0.02	-0.29	0.03
549		XMMU J105216.9+573843	10 52 16.99	57 38 43.6	1.1	42	35.7	4.9	0	0.7	0.7	39	35.0	4.8	4	31.4	10.1	0.77	0.20	-0.22	0.17
1595		XMMU J105217.4+573637	10 52 17.42	57 36 37.8	1.6	10	8.7	2.9	0	0.8	0.5	3	7.9	2.9	6	26.2	7.4	0.21	0.35	0.40	0.19
97		XMMU J105217.7+572127	10 52 17.72	57 21 27.1	1.3	13	11.7	3.1	2	1.4	0.6	6	10.4	3.0	5	22.6	7.0	0.09	0.25	0.21	0.20
196		XMMU J105218.8+572539	10 52 18.80	57 25 39.7	0.8	55	20.5	2.6	9	1.9	0.4	39	18.7	2.6	7	17.2	4.6	0.23	0.13	-0.21	0.14
91		XMMU J105218.8+572056	10 52 18.83	57 20 56.4	1.4	21	18.8	3.5	4	1.7	0.6	16	17.1	3.4	2	16.7	7.0	0.23	0.19	-0.18	0.22
413		XMMU J105219.4+573253	10 52 19.47	57 32 53.9	0.8	76	12.7	2.3	73	5.7	0.6	4	7.0	2.3	0	6.8	4.4	-0.67	0.09	-0.19	0.35
554		XMMU J105219.4+573903	10 52 19.47	57 39 3.4	0.7	198	45.2	4.7	170	15.7	1.1	30	29.5	4.5	0	10.9	9.5	-0.54	0.06	-0.59	0.29
107		XMMU J105219.6+572213	10 52 19.70	57 22 13.5	0.3	698	69.8	4.2	539	22.2	1.0	130	47.6	4.1	30	51.1	7.7	-0.49	0.04	-0.14	0.08
125	607	XMMU J105220.1+572306	10 52 20.17	57 23 6.8	0.4	483	50.1	3.5	406	17.2	0.9	77	32.9	3.4	2	12.6	5.6	-0.54	0.04	-0.57	0.15
1499		XMMU J105220.5+572942	10 52 20.53	57 29 42.5	1.2	18	8.7	2.0	14	2.1	0.4	5	6.5	2.0	0	0.0	1.1	-0.34	0.16	-1.00	0.23
525		XMMU J105222.4+573735	10 52 22.48	57 37 35.0	0.3	1016	47.0	3.5	1019	39.1	1.4	2	8.0	3.2	0	0.9	4.1	-0.94	0.02	-0.85	0.62
1526		XMMU J105222.7+573303	10 52 22.71	57 33 3.7	1.6	11	8.7	2.3	0	0.2	0.3	8	8.4	2.3	5	15.4	4.8	0.71	0.34	0.13	0.20
1233		XMMU J105223.2+572946	10 52 23.24	57 29 46.8	1.1	27	8.2	2.0	24	3.0	0.5	3	5.2	1.9	0	6.3	3.7	-0.57	0.14	-0.08	0.35
591		XMMU J105223.3+574121	10 52 23.36	57 41 21.6	0.4	847	112.2	7.3	778	50.1	2.0	64	62.1	7.0	7	56.3	15.0	-0.67	0.03	-0.22	0.14
188		XMMU J105223.9+572531	10 52 23.93	57 25 31.4	0.3	394	34.3	2.8	351	13.5	0.7	46	20.8	2.7	0	4.3	4.1	-0.61	0.04	-0.74	0.21
24		XMMU J105224.3+571739	10 52 24.36	57 17 39.8	0.9	62	28.5	4.8	54	8.8	1.0	10	19.7	4.7	0	8.2	9.4	-0.48	0.10	-0.55	0.41
321	23	XMMU J105224.6+573008	10 52 24.69	57 30 9.0	0.2	2075	95.4	3.7	1696	33.2	0.9	334	62.1	3.6	46	40.3	5.1	-0.54	0.02	-0.37	0.06
105		XMMU J105225.0+572155	10 52 25.01	57 21 55.5	1.2	18	12.6	3.0	13	2.8	0.6	6	9.8	2.9	0	7.1	5.8	-0.29	0.17	-0.32	0.39
120		XMMU J105225.2+572305	10 52 25.22	57 23 5.3	0.2	344	123.0	4.6	287	51.5	1.3	50	71.5	4.4	8	45.6	6.8	-0.64	0.02	-0.38	0.07
999	870	XMMU J105225.3+572247	10 52 25.34	57 22 47.3	0.4	359	44.0	3.6	305	17.1	0.9	47	26.9	3.5	8	23.5	6.0	-0.60	0.04	-0.24	0.13
199		XMMU J105225.5+572550	10 52 25.50	57 25 50.7	0.2	1010	102.4	4.2	353	13.1	0.7	573	89.3	4.1	84	61.0	6.0	0.04	0.04	-0.35	0.05
499		XMMU J105225.5+573605	10 52 25.59	57 36 5.9	1.0	50	16.7	3.0	40	4.9	0.7	9	11.8	2.9	1	13.0	6.3	-0.45	0.11	-0.13	0.27
50		XMMU J105225.8+571906	10 52 25.88	57 19 6.7	0.6	252	46.9	4.5	217	16.2	1.1	38	30.8	4.3	0	10.1	8.9	-0.54	0.06	-0.63	0.27
2141		XMMU J105227.0+573320	10 52 27.00	57 33 20.4	1.4	13	13.0	2.6	4	1.6	0.5	9	11.4	2.6	0	9.2	4.7	0.04	0.19	-0.27	0.26
427		XMMU J105227.9+573330	10 52 28.00	57 33 30.7	0.4	13	31.4	3.0	4	9.8	0.7	9	21.6	2.9	0	16.2	4.7	-0.48	0.06	-0.31	0.14
364		XMMU J105228.3+573104	10 52 28.34	57 31 4.3	0.3	69	44.7	2.8	67	17.8	0.8	4	26.8	2.7	0	24.4	4.5	-0.62	0.03	-0.22	0.10
577		XMMU J105228.7+574014	10 52 28.72	57 40 14.8	1.4	12	18.2	4.4	4	2.4	0.8	7	15.8	4.3	1	20.6	11.0	0.01	0.21	-0.04	0.30
2254		XMMU J105229.5+574332	10 52 29.51	57 43 32.6	1.0	60	106.9	25.6	59	46.9	6.1	3	60.0	24.8	0	58.3	54.7	-0.66	0.12	-0.19	0.49
482		XMMU J105229.7+573529	10 52 29.73	57 35 29.9	1.2	30	16.2	3.0	19	3.1	0.6	11	13.1	3.0	0	6.7	5.6	-0.20	0.14	-0.47	0.34
317		XMMU J105229.8+572947	10 52 29.88	57 29 47.2	0.9	40	13.8	2.3	28	3.2	0.5	14	10.7	2.3	0	0.0	2.8	-0.31	0.12	-1.00	0.36
2086		XMMU J105230.0+573103	10 52 30.00	57 31 3.4	0.7	69	14.2	2.3	67	6.4	0.6	4	7.9	2.2	0	0.0	2.7	-0.67	0.08	-1.00	0.49
553	2	XMMU J105230.0+573914	10 52 30.10	57 39 14.1	0.1	11794	487.8	9.6	10324	211.3	2.9	1312	276.6	9.2	159	187.3	14.1	-0.66	0.01	-0.35	0.04
340		XMMU J105231.1+573016	10 52 31.12	57 30 16.2	0.7	108	25.9	2.8	13	2.2	0.5	63	23.7	2.7	33	34.3	5.0	0.26	0.11	0.01	0.09
2393		XMMU J105231.2+571547	10 52 31.29	57 15 47.2	2.0	11	22.4	5.7	6	3.7	1.0	6	18.7	5.6	0	9.5	11.8	-0.11	0.20	-0.47	0.50
435		XMMU J105231.6+573341	10 52 31.62	57 33 41.5	0.8	82	15.3	2.5	72	5.5	0.6	9	9.8	2.4	2	10.8	4.8	-0.56	0.09	-0.12	0.25
179		XMMU J105231.8+572500	10 52 31.85	57 25 0.6	0.5	286	50.7	3.4	58	5.0	0.6	176	45.7	3.4	52	48.5	5.8	0.18	0.06	-0.14	0.07
166		XMMU J105232.1+572428	10 52 32.18	57 24 28.2	0.4	660	90.9	4.3	87	6.4	0.6	456	84.5	4.3	117	79.3	6.8	0.35	0.05	-0.20	0.05
486		XMMU J105232.8+573543	10 52 32.81	57 35 43.9	1.1	54	24.5	3.3	19	3.4	0.6	31	21.1	3.2	4	19.1	6.2	-0.00	0.12	-0.22	0.17
192		XMMU J105232.9+572537	10 52 32.93	57 25 37.9	2.0	13	9.7	2.3	5	1.4	0.4	7	8.3	2.2	2	9.0	4.0	-0.02	0.20	-0.14	0.26
26		XMMU J105233.0+571749	10 52 33.07	57 17 49.3	0.7	200	51.9	5.4	160	15.5											

SRC #	XMM	R	IAU name	RA (J2000)		DEC		err hh mm ss	0.5–10.0 keV			0.5–2.0 keV			2.0–10.0 keV			5.0–10.0 keV			HR1		err	HR2	err
				°	'	"			\mathcal{L}	flux	err	\mathcal{L}	flux	err	\mathcal{L}	flux	err	\mathcal{L}	flux	err	HR1	err			
443			XMMU J105237.1+573400	10 52 37.18	57 34 0.4	0.3	16	85.6	4.3	15	15.0	0.8	2	70.6	4.2	0	56.3	6.6	-0.15	0.04	-0.28	0.06			
355			XMMU J105237.3+573103	10 52 37.35	57 31 3.7	0.2	1561	88.2	3.7	1252	30.0	0.9	287	58.2	3.6	24	28.7	4.8	-0.53	0.02	-0.48	0.07			
424			XMMU J105238.1+573321	10 52 38.12	57 33 21.9	0.2	1859	171.2	5.5	415	16.4	0.8	1153	154.8	5.4	291	136.3	8.1	0.20	0.03	-0.23	0.03			
2297			XMMU J105238.5+571644	10 52 38.51	57 16 44.4	1.5	22	28.9	5.5	10	4.2	1.0	12	24.7	5.4	1	22.4	12.6	-0.04	0.16	-0.22	0.29			
1495			XMMU J105239.4+572842	10 52 39.49	57 28 42.2	1.7	16	7.6	1.9	12	1.9	0.4	4	5.7	1.8	0	5.9	3.5	-0.36	0.17	-0.15	0.33			
148	32		XMMU J105239.7+572431	10 52 39.76	57 24 31.5	0.1	102046	1413.9	11.4	87917	633.0	3.6	12131	780.9	10.8	1999	434.1	12.0	-0.67	0.00	-0.44	0.01			
610			XMMU J105239.8+574310	10 52 39.89	57 43 10.4	1.0	89	70.9	12.7	88	34.1	3.5	4	36.8	12.2	0	0.0	11.8	-0.71	0.09	-1.00	0.45			
468			XMMU J105241.0+573448	10 52 41.08	57 34 48.2	1.0	43	21.7	3.1	13	2.6	0.5	29	19.1	3.0	2	11.7	5.1	0.08	0.13	-0.40	0.19			
2378			XMMU J105241.4+573229	10 52 41.44	57 32 29.7	1.5	39	7.2	2.0	42	4.6	0.6	0	2.6	1.9	0	1.4	2.6	-0.84	0.11	-0.45	0.82			
131			XMMU J105241.6+572320	10 52 41.61	57 23 20.9	0.8	41	10.5	2.3	40	4.3	0.6	3	6.2	2.2	0	0.0	4.3	-0.63	0.12	-1.00	0.98			
505		104	XMMU J105241.6+573650	10 52 41.65	57 36 50.2	0.1	6575	392.6	8.9	4511	101.5	2.0	1802	291.1	8.7	263	194.6	12.1	-0.38	0.02	-0.36	0.03			
350			XMMU J105241.7+573038	10 52 41.78	57 30 38.1	0.4	456	44.9	3.0	344	12.3	0.7	109	32.6	2.9	4	12.1	3.9	-0.41	0.04	-0.59	0.11			
521			XMMU J105242.3+573717	10 52 42.33	57 37 17.9	0.7	73	39.4	4.6	22	4.7	0.8	46	34.7	4.6	5	29.0	8.7	0.08	0.11	-0.26	0.15			
385		14	XMMU J105242.3+573158	10 52 42.38	57 31 58.3	0.1	5765	232.1	5.4	3967	60.8	1.2	1580	171.3	5.3	219	97.2	6.5	-0.38	0.02	-0.43	0.03			
54			XMMU J105242.4+571913	10 52 42.46	57 19 14.0	1.5	16	4.2	2.9	18	4.2	0.8	0	0.0	2.8	0	8.2	8.5	-1.00	0.21	1.00	0.97			
289			XMMU J105242.7+572910	10 52 42.72	57 29 10.1	0.6	163	25.5	2.4	114	6.2	0.5	49	19.2	2.4	1	6.2	3.4	-0.34	0.07	-0.63	0.17			
1461			XMMU J105242.7+572847	10 52 42.76	57 28 47.6	1.5	11	2.1	1.5	14	2.1	0.4	0	0.0	1.4	0	0.0	0.8	-1.00	0.21	^a	^a			
5	52		XMMU J105243.2+571545	10 52 43.23	57 15 45.3	0.1	96	278.5	9.9	36	121.1	2.8	60	157.4	9.5	1	93.7	17.9	-0.66	0.02	-0.41	0.08			
2187			XMMU J105243.2+571722	10 52 43.28	57 17 22.2	0.9	39	31.0	5.3	27	7.6	1.1	11	23.5	5.2	1	25.5	11.9	-0.34	0.12	-0.13	0.25			
254		486	XMMU J105243.5+572759	10 52 43.51	57 27 59.5	0.2	1541	98.1	3.9	1091	26.3	0.9	399	71.8	3.8	52	43.1	5.2	-0.40	0.03	-0.40	0.06			
2379			XMMU J105243.5+572504	10 52 43.55	57 25 4.7	1.0	52	19.1	2.6	26	3.6	0.6	25	15.6	2.6	1	9.2	4.2	-0.19	0.11	-0.41	0.20			
1235			XMMU J105243.5+571607	10 52 43.57	57 16 7.2	0.8	97	70.0	7.2	36	8.8	1.2	60	61.2	7.1	1	29.8	14.5	0.05	0.09	-0.49	0.19			
489			XMMU J105243.7+573546	10 52 43.77	57 35 46.8	0.7	116	21.8	3.0	99	7.9	0.7	14	13.9	3.0	4	17.5	6.0	-0.56	0.08	-0.06	0.20			
322			XMMU J105243.7+572947	10 52 43.79	57 29 48.0	1.1	27	12.0	2.2	18	2.6	0.5	11	9.4	2.2	0	0.0	3.4	-0.27	0.14	-1.00	0.51			
465			XMMU J105244.2+573442	10 52 44.23	57 34 42.2	0.8	61	16.5	2.7	45	4.5	0.6	13	11.9	2.6	3	14.3	5.0	-0.41	0.10	-0.09	0.21			
15			XMMU J105244.2+571710	10 52 44.28	57 17 10.5	0.8	59	37.8	5.2	39	8.5	1.0	16	29.4	5.1	4	31.6	11.8	-0.29	0.10	-0.14	0.20			
502			XMMU J105244.7+573613	10 52 44.75	57 36 13.6	1.6	10	2.7	1.4	12	2.7	0.6	0	0.0	1.2	0	0.0	5.2	-1.00	0.15	^a	^a			
23	47		XMMU J105244.9+571733	10 52 44.92	57 17 33.6	0.9	40	31.3	4.7	28	13.3	1.1	12	18.0	4.5	1	9.3	9.9	-0.65	0.08	-0.46	0.43			
96		814	XMMU J105244.9+572122	10 52 44.92	57 21 22.2	0.2	298	108.1	4.9	253	44.6	1.3	41	63.5	4.7	5	47.7	7.9	-0.63	0.02	-0.31	0.08			
2514			XMMU J105245.5+574042	10 52 45.54	57 40 42.0	2.0	23	11.8	4.1	26	8.1	1.3	1	3.6	3.9	1	10.6	10.8	-0.87	0.13	0.34	0.65			
532		801	XMMU J105245.6+573745	10 52 45.63	57 37 45.8	0.6	284	34.6	3.7	273	18.3	1.1	14	16.3	3.5	0	0.0	7.1	-0.75	0.05	-1.00	0.61			
139			XMMU J105245.7+572329	10 52 45.78	57 23 29.7	0.6	12	3.6	1.3	11	2.8	0.5	0	0.8	1.2	2	12.6	5.1	-0.91	0.13	0.84	0.24			
2513			XMMU J105245.8+574033	10 52 45.84	57 40 33.0	2.0	80	26.4	4.8	81	14.5	1.4	5	11.9	4.6	1	11.8	10.5	-0.77	0.08	-0.18	0.47			
334			XMMU J105246.2+573009	10 52 46.22	57 30 9.5	0.8	74	13.4	2.2	67	4.8	0.5	9	8.6	2.1	0	0.6	2.0	-0.56	0.09	-0.91	0.31			
279			XMMU J105246.3+572820	10 52 46.37	57 28 20.5	1.2	35	17.5	2.5	1	0.8	0.4	34	16.6	2.4	1	7.6	3.9	0.53	0.18	-0.51	0.20			
2029			XMMU J105246.6+572105	10 52 46.62	57 21 5.7	0.5	102	34.2	4.2	85	12.3	1.1	18	21.9	4.0	1	17.3	7.3	-0.56	0.07	-0.28	0.21			
2512	840		XMMU J105247.0+574044	10 52 47.04	57 40 44.0	2.0	110	23.4	4.5	114	16.9	1.4	2	6.5	4.3	0	0.0	6.9	-0.89	0.07	-1.00	1.49			
1289			XMMU J105247.0+574100	10 52 47.05	57 41 0.7	1.8	41	23.5	5.3	40	10.1	1.3	3	13.4	5.2	0	5.7	9.0	-0.65	0.12	-0.54	0.57			
390			XMMU J105247.1+573200	10 52 47.11	57 32 0.4	1.0	45	7.7	2.0	46	4.3	0.5	1	3.4	2.0	0	0.0	3.7	-0.78	0.12	-1.00	1.51			
503			XMMU J105247.9+573620	10 52 47.93	57 36 20.9	0.6	123	25.9	3.3	29	4.2	0.6	33	21.7	3.2	61	71.6	8.0	-0.10	0.10	0.40	0.08			
481			XMMU J105248.0+573531	10 52 48.01	57 35 31.2	1.7	11	4.5	2.3	13	2.4	0.5	0	2.1	2.2	0	1.1	3.2	-0.76	0.23	-0.47	1.22			
448			XMMU J105248.0+573407	10 52 48.01	57 34 7.4	0.4	307	33.2	3.1	265	12.0	0.7	37	21.3	3.0	6	17.8	5.1	-0.56	0.05	-0.26	0.15			
90	37		XMMU J105248.2+572116	10 52 48.21	57 21 16.7	0.2	108	207.5	6.4	89	90.8	1.9	20	116.7	6.1	0	70.3	9.0	-0.66	0.02	-0.40	0.06			
1312			XMMU J105248.4+574128	10 52 48.42	57 41 28.8	0.4	483	104.5	7.9	425	41.1	2.1	59	63.4	7.6	2	33.9	15.4	-0.61	0.04	-0.45	0.19			
594			XMMU J105249.5+573209	10 52 49.59	57 32 9.3	1.2	13	6.4	2.1	10	2.0	0.5	1	4.4	2.0	2	9.5	4.0	-0.49	0.20	0.21	0.30			
74		905	XMMU J105251.1+572013	10 52 51.16	57 20 13.3	0.6	201	29.0	3.6	191	13.8	1.0	11	15.2	3.5	0	9.9	7.2	-0.70	0.06	-0.37	0.33			
394			XMMU J105251.4+573200	10 52 51.48	57 32 0.2	0.4	185	41.7	3.0	127	14.2</														

SRC #	XMM R	IAU name	RA (J2000)	DEC	err	0.5–10.0 keV			0.5–2.0 keV			2.0–10.0 keV			5.0–10.0 keV			HR1	err	HR2	err
			hh mm ss	° ' "	"	\mathcal{L}	flux	err	\mathcal{L}	flux	err	\mathcal{L}	flux	err	\mathcal{L}	flux	err				
403		XMMU J105257.1+573235	10 52 57.13	57 32 35.6	0.5	198	21.8	2.5	181	8.8	0.6	19	13.0	2.4	0	2.1	3.0	-0.62	0.06	-0.79	0.26
176	30	XMMU J105257.3+572507	10 52 57.32	57 25 7.3	0.1	5813	180.8	4.8	5179	82.2	1.5	593	98.6	4.6	43	44.6	5.9	-0.68	0.01	-0.52	0.05
19		XMMU J105257.3+571729	10 52 57.39	57 17 29.7	1.2	30	27.8	5.0	17	4.9	0.9	13	22.9	4.9	0	17.6	11.1	-0.15	0.14	-0.30	0.30
2375		XMMU J105257.3+574152	10 52 57.40	57 41 52.8	0.6	186	83.7	8.1	161	39.0	2.8	24	44.7	7.6	2	46.6	18.8	-0.69	0.05	-0.15	0.21
569		XMMU J105257.5+573947	10 52 57.56	57 39 47.8	1.2	21	24.5	4.5	0	1.1	0.7	18	23.5	4.5	3	28.3	10.0	0.55	0.24	-0.08	0.20
121	434	XMMU J105258.3+572251	10 52 58.32	57 22 51.0	0.3	842	69.8	4.0	723	25.4	1.0	116	44.4	3.9	4	18.1	5.7	-0.57	0.03	-0.55	0.11
1291		XMMU J105258.4+573102	10 52 58.42	57 31 2.2	1.0	36	11.2	2.3	0	0.0	0.2	15	11.1	2.3	22	27.1	4.6	0.97	0.22	0.26	0.12
153		XMMU J105258.5+572355	10 52 58.52	57 23 56.0	0.4	104	51.5	3.5	90	16.7	0.8	14	34.8	3.4	1	16.9	5.0	-0.50	0.04	-0.49	0.12
433		XMMU J105258.8+573334	10 52 58.89	57 33 34.8	0.6	145	23.2	2.7	119	7.4	0.6	25	15.7	2.6	2	9.7	4.3	-0.50	0.07	-0.39	0.20
447		XMMU J105258.9+573358	10 52 58.94	57 33 58.9	1.2	27	3.7	1.9	30	3.7	0.6	0	0.0	1.8	0	4.3	-1.00	0.15	-a	-a	
332	77	XMMU J105259.1+573030	10 52 59.19	57 30 30.2	0.1	1526	254.1	5.3	1072	85.9	1.4	361	168.2	5.1	94	118.8	6.8	-0.53	0.01	-0.33	0.03
278		XMMU J105259.3+572831	10 52 59.32	57 28 31.0	0.7	96	7.8	1.9	99	6.0	0.5	0	1.8	1.9	0	0.0	0.7	-0.91	0.09	-1.00	0.51
387	15	XMMU J105259.8+573155	10 52 59.89	57 31 55.1	0.3	1020	57.5	3.1	910	23.7	0.9	111	33.8	3.0	2	8.8	3.9	-0.63	0.03	-0.69	0.12
48		XMMU J105259.9+571900	10 52 59.94	57 19 0.3	1.0	25	18.6	3.6	17	4.1	0.8	10	14.5	3.5	0	3.0	5.9	-0.28	0.14	-0.75	0.44
34		XMMU J105300.8+571812	10 53 0.88	57 18 12.4	0.9	67	31.6	4.7	52	8.0	1.0	17	23.6	4.6	0	8.8	9.3	-0.36	0.10	-0.58	0.35
597		XMMU J105300.9+574208	10 53 0.99	57 42 8.5	0.1	35165	1283.9	14.5	35120	1204.2	10.5	53	79.7	10.0	0	3.8	12.0	-0.98	0.00	-0.93	0.20
607		XMMU J105301.6+571459	10 53 1.64	57 14 60.0	0.5	576	188.6	12.9	482	61.0	2.9	92	127.7	12.6	4	72.6	24.4	-0.50	0.04	-0.43	0.14
1527		XMMU J105302.0+574012	10 53 2.09	57 40 12.1	1.5	14	22.4	4.8	0	1.1	0.8	13	21.4	4.7	2	25.4	11.1	0.52	0.27	-0.09	0.24
2015		XMMU J105302.1+573032	10 53 2.17	57 30 32.1	0.8	105	21.1	2.6	78	5.7	0.6	26	15.4	2.5	1	7.3	3.9	-0.40	0.08	-0.50	0.21
527	5	XMMU J105302.5+573756	10 53 2.52	57 37 56.7	0.2	4274	223.8	6.8	3695	89.7	1.9	514	134.1	6.5	67	93.2	10.2	-0.62	0.02	-0.34	0.05
2838		XMMU J105302.8+573055	10 53 2.90	57 30 55.9	0.5	15	5.3	2.2	12	2.4	0.5	3	2.8	2.1	0	0.0	2.3	-0.69	0.20	-1.00	1.17
60		XMMU J105303.5+571936	10 53 3.52	57 19 36.3	1.4	12	13.5	3.4	7	2.7	0.7	5	10.8	3.4	0	10.0	7.9	-0.22	0.19	-0.21	0.40
476	827	XMMU J105303.5+573529	10 53 3.53	57 35 29.5	0.4	384	48.9	3.9	316	16.8	0.9	57	32.1	3.8	12	29.6	6.6	-0.54	0.05	-0.21	0.12
300	426	XMMU J105303.8+572924	10 53 3.88	57 29 24.7	0.2	3169	136.6	4.4	2597	47.8	1.1	535	88.7	4.2	38	36.8	5.1	-0.55	0.02	-0.55	0.05
1415		XMMU J105304.0+573715	10 53 4.08	57 37 15.8	1.5	14	9.9	3.1	10	2.6	0.6	2	7.2	3.0	2	16.7	7.1	-0.40	0.20	0.24	0.28
145		XMMU J105304.6+572345	10 53 4.65	57 23 45.7	1.0	24	7.9	2.3	23	3.2	0.5	1	4.7	2.2	0	6.1	4.4	-0.63	0.15	-0.05	0.44
362		XMMU J105304.7+573100	10 53 4.71	57 31 0.4	2.2	14	5.0	2.1	16	2.7	0.5	0	2.3	2.1	0	0.0	2.0	-0.76	0.19	-1.00	1.19
2502		XMMU J105304.8+574105	10 53 4.87	57 41 5.6	2.0	100	1.9	3.6	2	1.9	1.1	0	0.0	3.5	2	25.9	16.1	-1.00	0.59	1.00	0.38
259		XMMU J105305.6+572810	10 53 5.66	57 28 10.1	0.2	1659	143.3	5.0	29	3.4	0.5	1065	139.8	5.0	566	180.1	8.1	0.73	0.04	-0.05	0.03
431		XMMU J105305.8+573330	10 53 5.80	57 33 30.4	1.0	31	17.3	2.9	11	2.2	0.5	20	15.1	2.8	1	9.6	4.8	0.04	0.15	-0.38	0.23
93		XMMU J105306.0+572112	10 53 6.04	57 21 12.6	1.9	11	11.7	3.0	7	2.3	0.6	5	9.4	2.9	0	0.0	4.4	-0.21	0.20	-1.00	0.65
450	477	XMMU J105306.0+573424	10 53 6.09	57 34 24.5	0.2	1423	80.7	4.0	1264	34.6	1.1	135	46.1	3.8	26	38.6	6.3	-0.65	0.03	-0.26	0.09
599	54	XMMU J105307.3+571505	10 53 7.37	57 15 5.1	0.4	938	216.0	13.2	823	82.5	3.3	102	133.5	12.8	15	119.0	24.4	-0.59	0.03	-0.23	0.11
477		XMMU J105308.0+573519	10 53 8.07	57 35 19.6	2.0	12	9.3	2.6	7	2.2	0.6	3	7.1	2.5	2	13.1	5.9	-0.32	0.20	0.13	0.28
2257		XMMU J105308.6+573437	10 53 8.65	57 34 37.1	1.1	16	10.5	2.7	11	2.5	0.6	4	8.0	2.6	1	9.7	5.5	-0.33	0.18	-0.08	0.32
270	120	XMMU J105309.3+572820	10 53 9.39	57 28 21.0	0.1	4573	135.0	4.0	4101	61.6	1.2	434	73.4	3.8	40	37.4	5.1	-0.68	0.01	-0.47	0.06
138		XMMU J105309.4+572330	10 53 9.40	57 23 30.2	1.0	44	12.6	2.6	42	4.6	0.6	5	8.0	2.5	0	0.0	3.1	-0.57	0.12	-1.00	0.54
1392		XMMU J105309.4+573723	10 53 9.49	57 37 23.4	1.3	17	17.6	3.6	0	0.0	0.5	16	17.6	3.6	2	19.7	7.8	1.00	0.36	-0.12	0.22
220		XMMU J105309.6+572634	10 53 9.63	57 26 34.2	0.9	51	8.8	2.1	52	4.4	0.5	2	4.5	2.0	0	0.0	3.2	-0.72	0.11	-1.00	1.00
86		XMMU J105309.7+572057	10 53 9.78	57 20 57.5	0.4	508	51.5	4.1	461	22.3	1.1	44	29.2	4.0	4	23.7	7.5	-0.66	0.04	-0.27	0.16
2515		XMMU J105309.8+574147	10 53 9.84	57 41 47.1	2.0	100	3.9	2.9	5	3.9	1.4	0	0.0	2.5	0	0.0	5.9	-1.00	0.20	-a	-a
497		XMMU J105311.1+573600	10 53 11.15	57 36 0.1	0.7	112	26.3	3.4	97	9.9	0.9	15	16.4	3.3	1	12.2	6.5	-0.58	0.07	-0.31	0.26
2147		XMMU J105311.3+573829	10 53 11.38	57 38 29.4	0.7	72	25.6	3.8	63	10.0	1.0	11	15.6	3.7	0	0.0	4.5	-0.61	0.08	-1.00	0.41
604		XMMU J105311.7+574216	10 53 11.70	57 42 16.1	0.6	686	170.8	11.1	582	66.7	3.1	88	104.1	10.7	17	127.1	24.3	-0.60	0.04	-0.07	0.11
124	634	XMMU J105311.8+572307	10 53 11.80	57 23 7.0	0.3	976	74.4	4.0	809	26.2	1.0	153	48.2	3.9	16	33.1	6.4	-0.55	0.03	-0.35	0.09
183	82	XMMU J105312.3+572506	10 53 12.37	57 25 6.4	0.2	2456	106.8	4.1	2156	45.6	1.2	266	61.3	3.9	35	41.3	5.9	-0.65	0.02	-0.36	0.07
453	804	XMMU J105312.4+573424	10 53 12.50	57 34 24.7	0.3	694	68.0	4.2	587	24.3	1.1	104	43.7	4.1	5	20.6	6.3	-0.56	0.04	-0.50	0.12
543		XMMU J105312.8+573818	10 53 12.86	57 38 18.3	0.5	72	52.0	5.0	59	11.8	1.0	13	40.2	4.9	1	36.9	9.6	-0.30	0.07	-0.21	0.14
339		XMMU J105313.0+573016	10 53 13.08	57 30 16.4	0.5	153	38.0	3.2	32	3.4	0.5	106	34.6	3.2	16	24.5	4.8	0.24	0.08	-0.33	0.10
197		XMMU J105313.1+572549	10 53 1																		

SRC #		RA (J2000)	DEC	err	0.5–10.0 keV	0.5–2.0 keV	2.0–10.0 keV	5.0–10.0 keV	HR1	err	HR2	err		
XMM	R	IAU name	hh mm ss	° ' "	\mathcal{L}	flux	err	\mathcal{L}	flux	err	\mathcal{L}	flux	err	
475	6	XMMU J105316.8+573550	10 53 16.86	57 35 50.9	0.1	91979	2154.7	17.9	72626	777.2	4.9	16338	1377.5	17.3
66		XMMU J105317.3+572010	10 53 17.38	57 20 11.0	0.8	101	21.9	3.6	98	11.1	1.0	5	10.7	3.4
103		XMMU J105317.8+572150	10 53 17.89	57 21 50.1	0.7	160	29.6	3.5	140	10.9	0.9	21	18.7	3.4
2353		XMMU J105318.6+572719	10 53 18.68	57 27 19.6	2.3	11	2.5	1.6	13	2.5	0.5	0	0.0	1.5
69	41	XMMU J105318.9+572044	10 53 18.97	57 20 44.7	0.3	967	72.5	4.7	945	45.7	1.6	25	26.9	4.4
39	45	XMMU J105319.0+571852	10 53 19.03	57 18 52.9	0.2	2189	181.7	7.3	1930	77.1	2.1	232	104.5	7.0
1537		XMMU J105319.3+571520	10 53 19.37	57 15 20.1	1.7	19	56.8	12.3	10	8.6	2.0	9	48.2	12.2
540		XMMU J105320.3+573806	10 53 20.31	57 38 6.9	1.0	32	14.4	3.9	32	6.4	0.9	1	8.0	3.8
384		XMMU J105321.6+573147	10 53 21.69	57 31 47.2	0.3	714	63.6	3.7	555	19.1	0.9	149	44.5	3.6
2509		XMMU J105321.9+573524	10 53 21.95	57 35 24.1	2.0	89	15.9	3.0	91	8.5	0.8	5	7.4	2.9
287	821	XMMU J105322.1+572852	10 53 22.18	57 28 52.2	0.3	677	51.8	3.2	568	18.5	0.8	103	33.3	3.1
572		XMMU J105322.2+574008	10 53 22.23	57 40 8.9	0.9	80	37.1	6.0	73	13.8	1.4	9	23.3	5.8
470		XMMU J105322.9+573501	10 53 22.97	57 35 1.1	0.7	68	16.3	2.9	60	6.3	0.7	6	10.0	2.8
25		XMMU J105323.5+571736	10 53 23.58	57 17 36.3	0.9	36	20.0	5.1	35	7.8	1.1	2	12.2	5.0
545		XMMU J105324.2+573828	10 53 24.26	57 38 28.5	0.8	64	21.3	4.0	60	8.4	0.9	6	12.9	3.9
267	428	XMMU J105324.6+572818	10 53 24.67	57 28 18.9	0.2	2324	109.2	4.2	1981	41.9	1.1	305	67.3	4.0
146		XMMU J105324.7+572348	10 53 24.78	57 23 48.2	1.4	10	7.3	2.6	9	2.2	0.5	1	5.1	2.5
1492		XMMU J105325.1+573202	10 53 25.11	57 32 2.3	1.3	11	2.5	1.2	14	2.5	0.5	0	0.0	1.1
305		XMMU J105325.5+572910	10 53 25.56	57 29 10.3	1.5	26	7.1	2.2	27	3.4	0.5	1	3.6	2.1
247		XMMU J105325.9+572740	10 53 25.91	57 27 40.9	1.8	17	11.1	2.4	10	2.1	0.5	8	8.9	2.4
1496		XMMU J105326.0+572035	10 53 26.07	57 20 35.8	0.8	10	4.8	2.5	12	3.5	0.8	0	1.3	2.4
1476		XMMU J105326.8+573904	10 53 26.86	57 39 4.7	1.4	17	23.1	4.7	7	3.1	0.8	11	20.0	4.6
102		XMMU J105326.8+572145	10 53 26.89	57 21 45.2	0.7	87	40.9	4.3	21	4.1	0.7	62	36.8	4.3
189		XMMU J105326.8+572521	10 53 26.90	57 25 21.7	0.5	129	38.2	3.5	13	2.5	0.5	92	35.7	3.5
459		XMMU J105327.2+573429	10 53 27.23	57 34 29.0	0.5	184	49.4	4.0	46	5.5	0.7	112	44.0	4.0
137		XMMU J105327.4+572335	10 53 27.41	57 23 35.9	0.5	216	33.5	3.6	189	12.2	0.9	27	21.3	3.5
488	815	XMMU J105328.6+573540	10 53 28.67	57 35 40.7	1.2	40	6.3	1.7	43	6.2	0.8	0	0.1	1.5
195		XMMU J105328.7+572537	10 53 28.74	57 25 37.8	1.0	39	18.0	2.9	25	3.8	0.6	15	14.2	2.8
2053		XMMU J105329.2+572046	10 53 29.27	57 20 46.7	1.0	85	21.8	3.9	84	10.8	1.0	2	10.9	3.7
85	38	XMMU J105329.5+572104	10 53 29.52	57 21 4.2	0.2	70	143.1	5.9	72	62.9	1.7	0	80.3	5.6
20		XMMU J105330.4+571731	10 53 30.50	57 17 31.1	0.6	217	90.3	7.3	119	16.0	1.3	93	74.4	7.2
563		XMMU J105330.9+573922	10 53 30.95	57 39 22.9	0.4	579	175.5	9.1	60	10.8	1.2	382	164.7	9.0
590		XMMU J105331.4+574113	10 53 31.42	57 41 13.9	0.9	69	47.9	7.7	57	16.0	1.9	11	31.8	7.5
84		XMMU J105331.6+572033	10 53 31.64	57 20 33.4	0.6	179	60.3	5.1	82	9.4	0.9	90	50.9	5.0
168	31	XMMU J105331.8+572454	10 53 31.84	57 24 54.3	0.1	22507	643.0	9.4	18931	256.9	2.8	3158	386.1	9.0
315		XMMU J105332.7+572942	10 53 32.75	57 29 42.9	1.0	28	9.0	2.3	25	3.3	0.5	2	5.7	2.3
487		XMMU J105333.4+573536	10 53 33.41	57 35 37.0	2.4	18	7.6	3.1	20	4.1	0.7	0	3.4	3.0
258		XMMU J105333.6+572812	10 53 33.67	57 28 12.4	2.1	10	6.4	2.4	10	2.2	0.5	1	4.2	2.3
116		XMMU J105334.7+572227	10 53 34.73	57 22 27.3	0.6	189	66.3	5.0	28	4.7	0.7	151	61.6	5.0
147		XMMU J105334.9+572344	10 53 34.97	57 23 44.0	0.9	51	21.9	3.3	35	5.0	0.7	18	16.9	3.2
191	29	XMMU J105335.1+572542	10 53 35.12	57 25 42.4	0.1	37756	913.1	11.0	31005	348.5	3.1	5824	564.5	10.6
1455		XMMU J105335.4+573334	10 53 35.46	57 33 34.6	1.5	11	9.7	2.8	9	2.4	0.6	3	7.3	2.7
518		XMMU J105336.3+573726	10 53 36.33	57 37 26.4	0.4	352	86.1	5.8	215	19.5	1.3	129	66.6	5.7
535	232	XMMU J105336.3+573801	10 53 36.33	57 38 1.0	0.1	22734	452.4	6.4	22713	422.0	4.2	28	30.4	4.8
28		XMMU J105336.3+571756	10 53 36.34	57 17 56.6	0.7	80	40.9	5.9	63	11.5	1.3	17	29.4	5.7
44		XMMU J105336.5+571846	10 53 36.52	57 18 46.2	0.8	81	22.9	4.6	75	11.6	1.2	3	11.3	4.5
409		XMMU J105336.8+573259	10 53 36.90	57 32 59.0	1.4	87	11.6	2.7	89	8.7	0.8	0	2.9	2.6
1501		XMMU J105337.1+574153	10 53 37.13	57 41 53.7	1.6	15	74.2	17.2	6	8.9	2.8	10	65.3	17.0
122		XMMU J105337.5+572247	10 53 37.50	57 22 47.4	0.8	63	24.3	3.6	47	6.2	0.8	17	18.1	3.5
562		XMMU J105338.1+573919	10 53 38.12	57 39 19.0	1.5	29	31.0	5.8	18	6.5	1.2	11	24.6	5.7
271		XMMU J105338.3+572811	10 53 38.32	57 28 12.0	1.3	16	11.2	2.7	12	2.6	0.6	5	8.7	2.7
511		XMMU J105338.3+573654	10 53 38.33	57 36 54.6	0.4	351	102.0	6.3	131	13.4	1.1	211	88.6	6.2
472	228	XMMU J105339.7+573520	10 53 39.78	57 35 20.2	0.4	1581	133.9	6.1	1411	58.3	1.8	162	75.6	5.8
342	16	XMMU J105339.8+573104	10 53 39.82	57 31 4.7	0.1	44056	937.6	10.8	38819	437.3	3.6	4646	500.3	10.3
144	131	XMMU J105340.1+572352	10 53 40.17	57 23 52.7	0.5	502	28.1	2.9	507	25.7	1.2	0	2.4	2.7
117		XMMU J105340.5+572230	10 53 40.51	57 22 30.8	1.0	50	28.8	4.0	21	4.2	0.7	28	24.6	3.9
2380		XMMU J105341.4+573024	10 53 41.42	57 30 24.7	1.0	37	20.6	3.2	18	3.8	0.7	19	16.8	3.2
58		XMMU J105341.9+571935	10 53 41.93	57 19 35.7	0.6	220	50.8	5.8	200	20.4	1.4	19	30.4	5.7
397		XMMU J105342.0+573220	10 53 42.06	57 32 20.1	0.7	123	39.7	4.1	48	6.2	0.8	58	33.5	4.0
190		XMMU J105344.3+572532	10 53 44.35	57 25 32.1	0.8	59	26.1	3.9	16	3.7	0.7	24	22.4	3.8
277	25	XMMU J105344.9+572840	10 53 44.97	57 28 40.5	0.1	7891	301.4	6.9	6554	111.2	1.9	1187	190.2	6.7

SRC #	XMM R	IAU name	RA (J2000)		DEC		err	0.5–10.0 keV			0.5–2.0 keV			2.0–10.0 keV			5.0–10.0 keV			HR1	err	HR2	err
			hh	mm	ss	°	'	"	\mathcal{L}	flux	err	\mathcal{L}	flux	err	\mathcal{L}	flux	err	\mathcal{L}	flux	err			
165		XMMU J105345.0+572419	10 53 45.01	57 24 19.5	1.7	13	12.1	3.2	9	2.6	0.6	4	9.5	3.2	0	5.8	6.3	-0.27	0.19	-0.40	0.48		
370		XMMU J105346.1+573104	10 53 46.18	57 31 4.4	1.1	37	9.6	2.8	39	5.3	0.7	0	4.3	2.7	0	3.3	4.6	-0.77	0.13	-0.30	0.69		
1544		XMMU J105346.2+573608	10 53 46.23	57 36 8.5	1.9	12	4.4	2.1	13	4.0	0.8	0	0.4	1.9	1	16.3	9.5	-0.97	0.14	0.93	0.31		
461	229	XMMU J105346.4+573510	10 53 46.47	57 35 10.8	0.3	932	94.3	5.9	888	50.5	1.9	48	43.8	5.6	0	6.0	7.3	-0.76	0.03	-0.83	0.20		
200		XMMU J105346.9+572606	10 53 46.90	57 26 6.2	0.3	856	76.0	4.5	741	29.4	1.2	105	46.6	4.3	11	35.3	7.9	-0.60	0.03	-0.30	0.11		
442	805	XMMU J105347.3+573350	10 53 47.37	57 33 50.0	0.4	668	84.1	5.1	543	27.7	1.3	122	56.4	5.0	4	25.7	8.3	-0.51	0.04	-0.51	0.12		
268		XMMU J105348.1+572816	10 53 48.15	57 28 16.3	0.3	761	109.9	5.4	382	19.3	1.0	336	90.6	5.3	43	61.6	8.1	-0.15	0.04	-0.35	0.06		
326	117	XMMU J105348.8+573034	10 53 48.84	57 30 34.2	0.1	8944	488.6	9.5	5360	106.2	1.9	2989	382.4	9.4	595	296.9	13.4	-0.27	0.01	-0.29	0.02		
383		XMMU J105348.9+573133	10 53 48.91	57 31 33.2	0.7	101	9.2	1.1	105	9.2	0.8	0	0.0	0.8	0	3.0	4.6	-1.00	0.03	1.00	0.73		
2020	27	XMMU J105350.2+572709	10 53 50.28	57 27 9.7	0.2	1607	171.5	6.5	1313	72.1	1.9	259	99.4	6.2	36	50.6	8.2	-0.64	0.02	-0.47	0.07		
2374		XMMU J105350.3+573000	10 53 50.33	57 30 0.4	1.3	19	5.6	2.2	19	4.0	0.7	0	1.6	2.1	1	13.5	6.4	-0.88	0.15	0.72	0.34		
452		XMMU J105350.4+573406	10 53 50.42	57 34 6.2	1.4	30	25.6	4.2	8	2.7	0.7	21	22.9	4.1	2	18.1	8.2	0.14	0.16	-0.28	0.22		
1551		XMMU J105350.7+572733	10 53 50.73	57 27 34.0	0.8	85	20.2	3.4	81	9.6	0.9	5	10.7	3.3	1	12.0	6.9	-0.70	0.08	-0.11	0.32		
182	128	XMMU J105350.8+572513	10 53 50.81	57 25 13.6	0.3	1316	114.1	5.5	1102	40.6	1.4	194	73.5	5.3	22	49.6	8.7	-0.55	0.03	-0.35	0.08		
508		XMMU J105351.5+573637	10 53 51.56	57 36 37.7	0.4	286	56.5	5.3	247	21.2	1.3	36	35.3	5.2	5	37.6	11.8	-0.58	0.05	-0.14	0.17		
222		XMMU J105351.7+572702	10 53 51.77	57 27 2.6	0.2	1627	268.3	7.8	1281	83.5	2.0	300	184.7	7.6	47	94.6	9.7	-0.48	0.02	-0.47	0.04		
438		XMMU J105352.1+573344	10 53 52.12	57 33 44.2	0.7	68	33.5	4.2	33	5.4	0.8	32	28.1	4.1	3	23.7	8.2	-0.10	0.10	-0.25	0.18		
35		XMMU J105352.9+571816	10 53 52.94	57 18 16.1	0.7	116	52.6	8.5	108	23.5	2.2	7	29.1	8.2	3	58.9	23.1	-0.67	0.08	0.18	0.23		
266		XMMU J105354.6+572804	10 53 54.59	57 28 4.3	1.0	39	26.0	3.8	6	2.2	0.6	30	23.8	3.7	3	18.7	7.2	-0.27	0.15	-0.29	0.19		
547		XMMU J105355.6+573842	10 53 55.69	57 38 42.4	0.2	1491	412.1	16.8	964	98.0	3.7	489	314.1	16.3	39	203.2	28.0	-0.33	0.03	-0.37	0.06		
206		XMMU J105355.9+572611	10 53 55.95	57 26 11.5	0.8	78	39.7	4.4	12	3.1	0.7	59	36.6	4.3	7	30.5	8.2	0.30	0.11	-0.26	0.14		
151		XMMU J105356.0+572356	10 53 56.03	57 23 56.4	0.6	108	46.2	4.9	2	1.7	0.7	70	44.5	4.8	37	79.7	11.1	0.62	0.13	0.12	0.09		
406	828	XMMU J105357.2+573241	10 53 57.20	57 32 41.8	0.2	1323	103.4	5.4	1186	45.3	1.5	116	58.1	5.2	23	56.2	9.6	-0.66	0.03	-0.19	0.09		
1487		XMMU J105357.5+572229	10 53 57.59	57 22 29.4	1.8	15	19.6	4.8	0	1.4	0.9	9	18.2	4.7	7	44.3	12.3	0.35	0.29	0.26	0.18		
304	861	XMMU J105358.3+572925	10 53 58.40	57 29 25.8	0.4	605	83.8	5.0	428	22.2	1.1	158	61.6	4.9	20	47.5	8.6	-0.39	0.04	-0.30	0.09		
299		XMMU J105358.8+572856	10 53 58.85	57 28 56.8	1.7	16	8.6	3.0	16	3.6	0.7	1	5.0	3.0	0	11.9	7.3	-0.64	0.18	0.26	0.40		
106		XMMU J105359.3+572157	10 53 59.32	57 21 57.7	1.4	29	37.7	6.1	8	4.2	1.1	22	33.6	6.0	0	10.2	11.8	0.12	0.16	-0.65	0.34		
203		XMMU J105359.9+572601	10 53 59.94	57 26 1.1	0.6	211	51.4	4.8	158	13.1	1.0	54	38.3	4.7	1	13.4	7.8	-0.37	0.06	-0.60	0.19		
454		XMMU J105400.2+573418	10 54 0.23	57 34 18.2	0.9	44	17.5	3.9	39	6.4	0.9	4	11.1	3.8	2	23.3	9.0	-0.57	0.12	0.19	0.25		
419		XMMU J105400.3+573232	10 54 0.39	57 33 22.8	0.3	1003	143.7	6.7	624	31.5	1.3	330	112.2	6.6	50	94.9	11.7	-0.28	0.03	-0.25	0.06		
1427		XMMU J105400.7+572850	10 54 0.73	57 28 50.0	1.7	13	17.2	3.6	1	1.0	0.6	12	16.1	3.5	0	10.8	7.1	0.42	0.24	-0.36	0.30		
1574		XMMU J105401.5+572815	10 54 1.57	57 28 16.0	2.3	10	14.6	3.6	0	0.9	0.6	8	13.7	3.5	2	18.0	7.9	0.41	0.29	-0.04	0.25		
119		XMMU J105402.5+572235	10 54 2.55	57 22 36.0	0.5	315	70.2	6.5	286	31.4	1.9	29	38.8	6.2	2	33.8	15.2	-0.67	0.05	-0.24	0.22		
2392		XMMU J105402.5+573650	10 54 2.58	57 36 50.4	1.5	11	12.1	5.1	11	5.0	1.1	0	7.1	5.0	0	16.2	13.8	-0.64	0.22	0.23	0.52		
1438		XMMU J105403.2+573024	10 54 3.25	57 30 24.4	2.0	13	7.7	3.1	14	3.5	0.7	0	4.1	3.0	0	0.0	4.5	-0.69	0.20	-1.00	1.54		
1304		XMMU J105403.9+572450	10 54 3.95	57 24 50.8	2.1	16	20.9	4.9	0	0.8	0.7	10	20.1	4.9	7	41.8	11.3	0.60	0.31	0.19	0.17		
78		XMMU J105404.3+572037	10 54 4.32	57 20 37.3	0.2	1413	163.8	8.9	1365	99.0	3.2	51	64.8	8.3	0	23.0	17.0	-0.81	0.02	-0.60	0.24		
1518		XMMU J105406.1+572413	10 54 6.17	57 24 13.4	1.3	12	23.4	5.1	0	0.7	0.8	13	22.7	5.0	0	17.0	11.6	0.68	0.33	-0.31	0.32		
421		XMMU J105406.8+573310	10 54 6.85	57 33 10.1	1.0	43	28.4	4.7	19	4.4	0.8	18	24.0	4.6	7	38.2	10.0	-0.07	0.13	0.06	0.16		
469		XMMU J105407.1+573525	10 54 7.16	57 35 25.3	0.1	10997	638.7	13.1	9676	287.0	4.2	1179	351.7	12.5	144	247.8	19.8	-0.67	0.01	-0.34	0.04		
331		XMMU J105407.5+573000	10 54 7.57	57 30 0.8	1.1	35	8.4	2.9	37	6.2	0.8	0	2.3	2.7	0	12.1	8.1	-0.89	0.13	0.58	0.46		
140		XMMU J105408.4+572337	10 54 8.44	57 23 37.6	1.3	31	35.7	6.0	11	5.1	1.2	19	30.6	5.9	2	32.5	14.2	-0.02	0.15	-0.14	0.23		
338	20	XMMU J105410.3+573038	10 54 10.31	57 30 38.5	0.1	1005	172.4	5.8	779	125.9	2.4	211	46.5	5.3	16	2.8	5.9	-0.89	0.01	-0.92	0.16		
2024		XMMU J105410.9+573057	10 54 11.00	57 30 57.4	0.2	1115	154.3	6.8	875	56.9	1.9	224	97.3	6.6	17	58.2	10.6	-0.57	0.03	-0.41	0.08		
2508		XMMU J105412.1+573420	10 54 12.15	57 34 20.1	2.0	100	0.5	2.1	0	0.5	0.7	0	0.0	2.0	0	0.0	11.2	-1.00	1.38	^a	^a		
1379		XMMU J105414.1+572744	10 54 14.14	57 27 44.9	1.6	29	36.5	5.8	4	2.8	1.0	26	33.7	5.7	1	21.7	11.5	0.31	0.17	-0.38	0.24		
429		XMMU J105414.2+573330	10 54 14.23	57 33 30.2	0.6	163	54.4	6.0	137	17.6	1.4	28	36.8	5.8	0	13.0	11.6	-0.50	0.07	-0.60	0.29		
218		XMMU J105414.3+572635	10 54 14.33	57 26 35.4	1.4	23	29.6	5.5	15	6.3	1.2	10	23.2	5.4	0	1.5	6.7	-0.27	0.14	-0.91	0.38		
185		XMMU J105415.2+572502	10 54 15.22	57 25 2.2	1.0	87	51.9	7.1	72	16.4	1.7	17	35										

Table 4. Catalogue of extended X-ray sources with likelihood of extent greater than 15.0 (5σ). Description of columns: (1) XMM-Newton source number as displayed in Fig. 3, (2) ROSAT source number (Lehmann et al. 2001), (3) IAU source name, (4–6) J2000 coordinates and errors, (7–8) likelihood of detection and likelihood of extent (rounded to nearest integer), (9) source extent (core radius of King profile), (10–11) fluxes and flux errors [10^{-16} erg cm $^{-2}$ s $^{-1}$] in 0.5–10 keV band, (12–15) hardness ratios and errors. All errors are 1σ errors.

SRC # XMM ^a	R	IAU name	RA (J2000) hh mm ss	DEC ° / ' / "	err "	\mathcal{L} detection	extent "	extent "	0.5–10.0 keV flux	err	HR1	err	HR2	err
395		XMMU J105151.6+573225	10 51 51.62	57 32 25.0	2.3	134	62	12.3	127.7	40.6	-0.75	0.15	-0.55	0.76
355		XMMU J105237.3+573104	10 52 37.30	57 31 04.5	0.3	1761	97	1.9	122.3	46.7	-0.53	0.02	-0.42	0.06
2378		XMMU J105242.1+573237	10 52 42.15	57 32 37.0	2.2	76	33	6.3	25.8	6.2	-0.94	0.08	-1.00	2.36
2512-	840	XMMU J105246.1+574044	10 52 46.18	57 40 44.8	1.5	376	134	9.7	217.4	22.8	-0.80	0.05	-0.56	0.46
2515														
476	827	XMMU J105303.4+573529	10 53 3.48	57 35 29.9	0.6	431	27	1.5	66.4	4.9	-0.50	0.04	-0.24	0.11
69	41	XMMU J105318.8+572045	10 53 18.87	57 20 45.1	0.7	1560	479	7.0	283.6	14.0	-0.78	0.02	-0.67	0.25
2394		XMMU J105319.9+573536	10 53 19.96	57 35 36.2	5.7	38	27	19.3	164.8	71.6	-0.91	0.16	-0.08	1.44
409		XMMU J105336.8+573257	10 53 36.89	57 32 57.4	1.5	125	41	4.1	26.2	6.0	-0.91	0.08	0.55	0.38
472	228	XMMU J105339.9+573522	10 53 39.94	57 35 22.6	0.5	2408	565	6.3	414.9	14.8	-0.64	0.02	-0.51	0.09
144	131	XMMU J105340.1+572352	10 53 40.10	57 23 52.2	0.6	565	39	1.8	41.5	4.4	-0.94	0.04	0.16	0.49
58		XMMU J105341.9+575525	10 53 41.98	57 19 36.8	0.9	235	18	1.9	83.3	7.9	-0.56	0.06	-0.29	0.20
461	229	XMMU J105346.5+573509	10 53 46.54	57 35 09.2	0.7	1463	534	12.2	759.0	34.7	-0.70	0.02	-0.88	0.16
185		XMMU J105416.2+572458	10 54 16.24	57 24 58.4	1.8	131	31	6.0	180.9	19.3	-0.50	0.06	-0.81	0.28

^a source number of corresponding object from point source detection list (Table 3), except for object 2394 not previously detected as a point source.

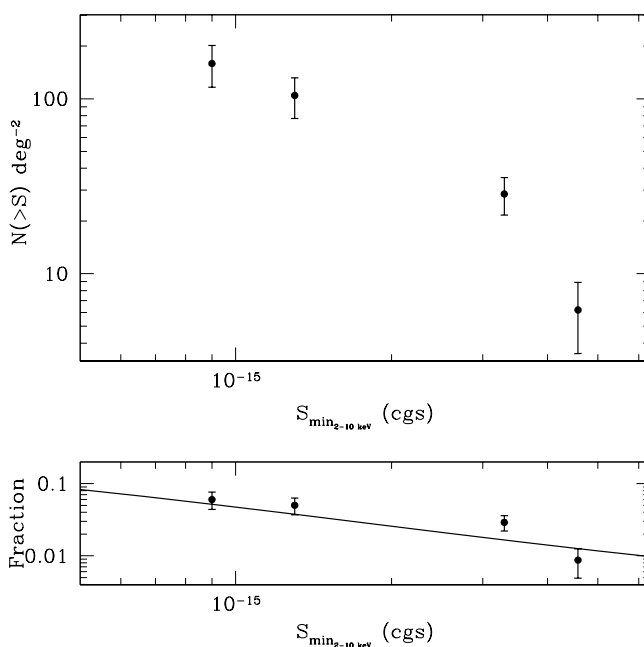


Fig. 8. *Upper panel:* The logN-logS of Compton thick source candidates as derived from the observed fraction rescaled to the expected number density at the flux of faintest source of the survey. From left to right: the Lockmann Hole (this paper), the CDFS (Tozzi et al. 2006), the XMM-COSMOS (Hasinger et al. 2007) and the *Chandra*-SWIRE survey (Polletta et al. 2006). *Lower panel:* The fraction of Compton thick source candidates in the Lockmann Hole, the CDFS, the XMM-COSMOS and *Chandra*-SWIRE, respectively from left to right. The solid lines represents the prediction of the X-ray background model by Gilli et al. (2006).

from the Spanish Ministry of Education and Science through project ESP2006-13608-C02-01.

References

- Bauer, F. E., Alexander, D. M., Brandt, W. N., Schneider, D. P., Treister, E., Hornschemeier, A. E., & Garmire, G. P. 2004, AJ, 128, 2048
- Baldi, A., Molendi, S., Comastri, A., Fiore, F., Matt, G., & Vignali, C. 2002, ApJ, 564, 190
- Cappelluti, N., Cappi, M., Dadina, M., Malaguti, G., Branchesi, M., D'Elia, V., & Palumbo, G. G. C. 2005, A&A, 430, 39
- Cappelluti, N., Hasinger, G., Brusa, M., et al. 2007, ApJS in press, ArXiv Astrophysics e-prints, arXiv:astro-ph/0701196
- Cash, W. 1979, ApJ, 228, 939
- Della Cecca, R., Maccacaro, T., Caccianiga, A., et al. 2004, A&A, 428, 383
- Eckart, M. E., Stern, D., Helfand, D. J., Harrison, F. A., Mao, P. H., & Yost, S. A. 2006, ApJS, 165, 19
- Fiore, F., Giommi, P., Vignali, C., et al. 2001, MNRAS, 327, 771
- Giacconi, R., Rosati, P., Tozzi, P., et al. 2001, ApJ, 551, 624
- Gilli, R., Comastri, A., & Hasinger, G. 2007, A&A, 463, 79
- Giommi, P., Perri, M., & Fiore, F. 2000, VizieR Online Data Catalog, 336, 20799
- Hashimoto, Y., Barcons, X., Boehringer, H., et al. 2004, A&A, 417, 819
- Hashimoto, Y., Henry, P. J., Hasinger, G., Szokoly, G., Schmidt, M., 2005, A&A, 439, 29
- Hasinger, G., Burg, R., Giacconi, R., Hartner, G., Schmidt, M., Trumper, J., & Zamorani, G. 1993, A&A, 275, 1
- Hasinger, G., Burg, R., Giacconi, R., et al. 1998, A&A, 329, 482
- Hasinger, G., Altieri, B., Arnaud, M., et al. 2001, A&A, 365, L45
- Hasinger, G., Miyaji, T., & Schmidt, M. 2005, A&A, 441, 417
- Hasinger, G., Cappelluti, N., Brunner, H., et al. 2007, ApJS in press, ArXiv Astrophysics e-prints, arXiv:astro-ph/0612311
- Kim, M., Wilkes, B. J., Kim, D.-W., Green, P. J., Barkhouse, W. A., Lee, M. G., Silverman, J. D., & Tananbaum, H. D. 2006, ArXiv Astrophysics e-prints, arXiv:astro-ph/0611841
- Lehmann, I., Hasinger, G., Schmidt, M., et al. 2001, A&A, 371, 833
- Lehmer, B. D., Brandt, W. N., Alexander, D. M., et al. 2005, ApJS, 161, 21
- Magdziarz, P., & Zdziarski, A. A. 1995, MNRAS, 273, 837
- Mainieri, V., Bergeron, J., Hasinger, G., et al. 2002, A&A, 393, 425
- Mainieri, V., Hasinger, G., Cappelluti, N., et al. 2007, ApJS in press, ArXiv Astrophysics e-prints, arXiv:astro-ph/0612361
- Mateos, S., Barcons, X., Carrera, F. J., et al. 2005, A&A, 433, 855
- Moretti, A., Campana, S., Lazzati, D., & Tagliaferri, G. 2003, ApJ, 588, 696
- Polletta, M. d. C., et al. 2006, ApJ, 642, 673
- Puccetti, S., Fiore, F., D'Elia, V., et al. 2006, A&A, 457, 501
- Murdoch, H. S., Crawford, D. F., & Jauncey, D. L. 1973, ApJ, 183, 1
- Rosati, P., Tozzi, P., Giacconi, R., et al. 2002, ApJ, 566, 667
- Tozzi, P., et al. 2006, A&A, 451, 457
- Szokoly, G., et al., in preparation
- Worsley, M. A., Fabian, A. C., Barcons, X., et al. 2004, MNRAS, 352, 28
- Worsley, M. A., Fabian, A. C., Bauer, D. M., et al. 2005, MNRAS, 357, 1281
- Yang, Y., Mushotzky, R. F., Barger, A. J., Cowie, L. L., Sanders, D. B., & Steffen, A. T. 2003, ApJ, 585, L85